Spinal macrophages resolve nociceptive hypersensitivity after peripheral injury

Jesse K. Niehaus,[1,2] Bonnie Taylor-Blake,[3] Lipin Loo,[3] Jeremy M. Simon,[1,4,5] and Mark J. Zylka[1,3,5,6,*]

[1]UNC Neuroscience Center, The University of North Carolina at Chapel Hill, Chapel Hill, NC 27599, USA
[2]Neuroscience Curriculum, The University of North Carolina at Chapel Hill, Chapel Hill, NC 27599, USA
[3]Department of Cell Biology and Physiology, The University of North Carolina at Chapel Hill, Chapel Hill, NC 27599, USA
[4]Department of Genetics, University of North Carolina at Chapel Hill, Chapel Hill, NC 27599, USA
[5]Carolina Institute for Developmental Disabilities, University of North Carolina at Chapel Hill, Chapel Hill, NC 27599, USA
[6]Lead contact
*Correspondence: zylka@med.unc.edu
https://doi.org/10.1016/j.neuron.2021.02.018

SUMMARY

Peripheral nerve injury induces long-term pro-inflammatory responses in spinal cord glial cells that facilitate neuropathic pain, but the identity of endogenous cells that resolve spinal inflammation has not been determined. Guided by single-cell RNA sequencing (scRNA-seq), we found that MRC1$^+$ spinal cord macrophages proliferated and upregulated the anti-inflammatory mediator *Cd163* in mice following superficial injury (SI; nerve intact), but this response was blunted in nerve-injured animals. Depleting spinal macrophages in SI animals promoted microgliosis and caused mechanical hypersensitivity to persist. Conversely, expressing *Cd163* in spinal macrophages increased *Interleukin 10* expression, attenuated micro- and astrogliosis, and enduringly alleviated mechanical and thermal hypersensitivity in nerve-injured animals. Our data indicate that MRC1$^+$ spinal macrophages actively restrain glia to limit neuroinflammation and resolve mechanical pain following a superficial injury. Moreover, we show that spinal macrophages from nerve-injured animals mount a dampened anti-inflammatory response but can be therapeutically coaxed to promote long-lasting recovery of neuropathic pain.

INTRODUCTION

Peripheral nerve injury induces a pro-inflammatory response in the spinal cord in rodents and humans and can cause chronic neuropathic pain (Albrecht et al., 2018; Costigan et al., 2009; Echeverry et al., 2017). Spinal microglia have traditionally been implicated in this pro-inflammatory response and, in males, promote persistent pain hypersensitivity (Griffin et al., 2007; Lacroix-Fralish et al., 2006b; Sorge et al., 2015; Uttam et al., 2018). However, treatments targeting pro-inflammatory mechanisms, particularly in microglia, were ineffective in patients with neuropathic pain (Eisenach et al., 2010; Ostenfeld et al., 2015; Vanelderen et al., 2015; Wang et al., 2014). These data raise the possibility that additional cell types might influence neuroimmune responses and pain hypersensitivity in neuropathic animals.

Single-cell RNA sequencing (scRNA-seq) studies indicate that the central nervous system (CNS) is composed of highly heterogeneous cell types (Sathyamurthy et al., 2018; Zeisel et al., 2018). Given the cellular complexity of the CNS, of which the spinal cord is a part, we sought to more comprehensively identify additional cellular responses that occur in a model of neuropathic pain (Shields et al., 2003). Here, we hypothesized that a more comprehensive understanding of which spinal cell types respond, or fail to respond, following nerve injury may reveal new regulators of pain hypersensitivity and new therapeutic targets for neuropathic pain.

RESULTS

Classification of spinal cell types in superficially injured and nerve-injured animals using scRNA-seq

The spared nerve injury (SNI) model of neuropathic pain produces long-lasting cellular and molecular changes in the spinal cord as well as mechanical allodynia compared with superficial tissue-injured (SI; also commonly referred to as sham-injured) controls, where mechanical allodynia resolves within 7 days (Figure S1A; Shields et al., 2003). To more comprehensively evaluate long-term cellular changes following superficial tissue injury versus nerve injury, we performed scRNA-seq on lumbar spinal cord segments from adult male mice 14 days post-injury (dpi; SI versus SNI; n = 10 and n = 9 replicates, respectively; Figures 1A and 1B). We sequenced ~20,000 total cells and performed unsupervised cell clustering, which detected 66 cell types that were hierarchically categorized into seven principal cell types (Loo et al., 2019; Figures 1C, 1D, and S1B–S1E). We characterized cell types using marker genes from mousebrain.org (Zeisel et al., 2018) and used binomial testing to identify three (or fewer) genes that molecularly distinguished each of the 66 cell types (Figures S2A and S2B; Table S1). There was a strong correlation between spinal neuron cell types in our dataset and previously published scRNA-seq datasets (Häring et al., 2018; Sathyamurthy et al., 2018; Figure S2C). Our data are accessible as an online web application at https://zylkalab.org/data, which plots

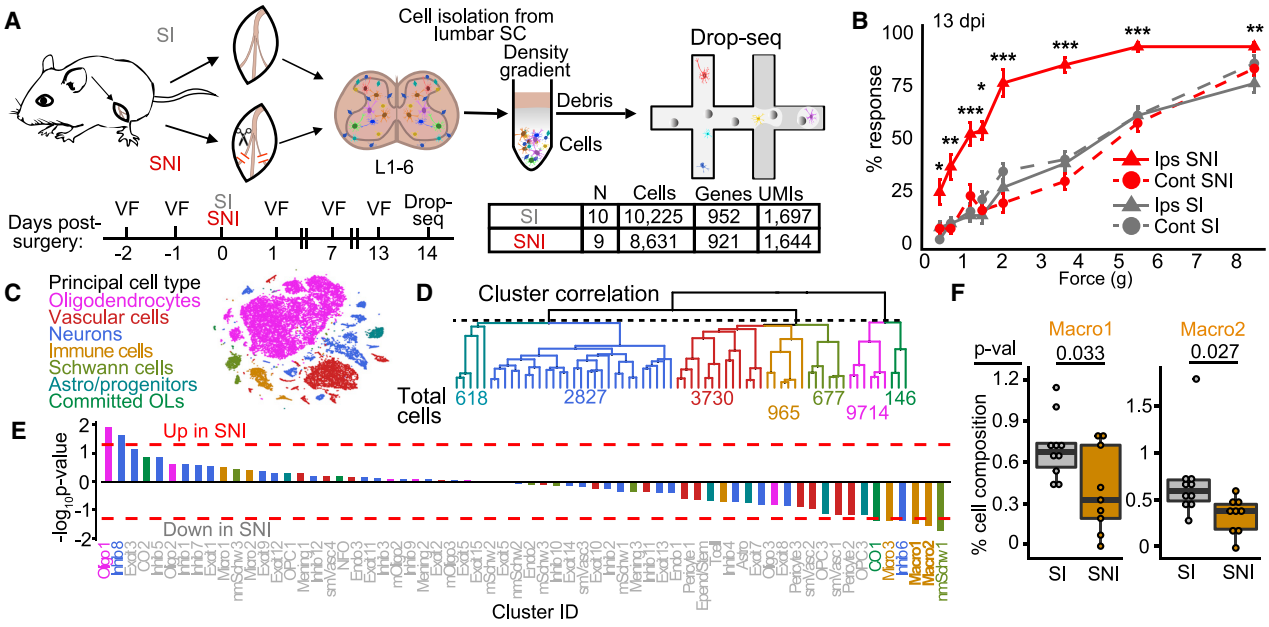

Figure 1. Classification of lumbar spinal cord cell types in superficially injured and nerve-injured animals using scRNA-seq

(A) Experimental outline and scRNA-seq summary table (median genes/UMIs per cell). VF, von Frey mechanical sensitivity testing.

(B) Mechanical sensitivity 13 dpi (n = 10 male mice per SI/SNI group). Mean ± SEM. Bonferroni-Holm-corrected two-sided Student's t tests. *p < 0.05, **p < 0.01, and ***p < 0.001. See Figure S1A for sensitivity over time.

(C) t-distributed stochastic neighbor embedding (tSNE) plot of principal cell types. See Figure S1E for tSNE plots of marker gene expression.

(D) Dendrogram showing relationships of 66 cell types on the basis of average gene expression. Dashed line used to define principal cell types, Pearson's distance = 1. See Figures S2A and S2B and Table S1 for cell-specific marker genes.

(E) Cell proportion differences between SI (n = 10) and SNI (n = 9) mice across all 66 cell types. Red dashed line indicates $-\log_{10}(p = 0.05)$, two-sided Student's t tests.

(F) Macro1 and Macro2 cellular proportions in SI (n = 10) and SNI (n = 9) animals, from scRNA-seq data. p values calculated from two-sided Student's t test. Consecutive datapoints within 1/30th of the range are binned.

user-directed gene expression across all cell types from SI and SNI animals 14 dpi.

Expansion and proliferation of spinal macrophages are blunted in nerve-injured animals

We then evaluated changes in cell proportions between SI and SNI animals (Figures 1E and 1F). Two of the six cell types significantly reduced in SNI animals were highly similar macrophage cell types (Macro1, Macro2) that express the macrophage mannose receptor (*Mrc1*; also known as MMR or CD206) and lack expression of microglia-specific genes *Tmem119* and *Siglech* (Bennett et al., 2016; Konishi et al., 2017; Figures S2B and S3A). Unlike spinal microglia, little is known about spinal macrophages in neuropathic pain mechanisms. Macro1 and Macro2 expressed genes associated with border associated macrophages (Figure S3A): antigen-presenting neuroimmune cells that localize along the edges of connective tissue in the CNS (Van Hove et al., 2019). Macro1 expressed higher levels of *Ccr2*, suggesting that these cells are peripherally derived and may represent macrophages in the dorsal roots (Stratton et al., 2018). Indeed, we detected MRC1$^+$ macrophages in the subdural meninges that surround the spinal cord (meningeal macrophages [MMs]), in the spinal perivascular space (perivascular macrophages [PVMs]), and within the dorsal root (Figures S3B and S3C; Goldmann et al., 2016). The majority of IBA1$^+$ microglia were MRC1$^-$ (Figure S3D), which is consistent with our scRNA-seq data (Figure S3A) and previous studies (Jordão et al., 2019; Ruan et al., 2020). We focused subsequent analyses on spinal MMs and PVMs because they could be reproducibly identified and quantified on the basis of markers and anatomical location (Figure S3B).

The neuroimmune response in the spinal cord following peripheral nerve injury is temporally dynamic in terms of both cellular composition and molecular phenotypes (Echeverry et al., 2017; Zhang and De Koninck, 2006). To investigate whether spinal macrophages undergo a dynamic response following peripheral injury, we quantified the number of MRC1$^+$ MMs and PVMs in naive (non-injured) animals and at 1, 3, 7, and 14 dpi in SI and SNI animals.

We detected a significant interaction between time post-injury and both MM and PVM numbers (Figures 2A, 2B, S3E, and S3F). MM expansion was blunted in SNI animals compared with SI animals, whereas PVMs did not differ by type of injury (SI, SNI; Figure 2B). Pairwise Tukey post hoc tests revealed that both MM and PVM populations increase following SI relative to naive animals (7 dpi for MMs, 14 dpi for PVMs), whereas neither cell type expanded from baseline in SNI animals (Figures 2A, S3E, and S3F). We did not detect a difference in

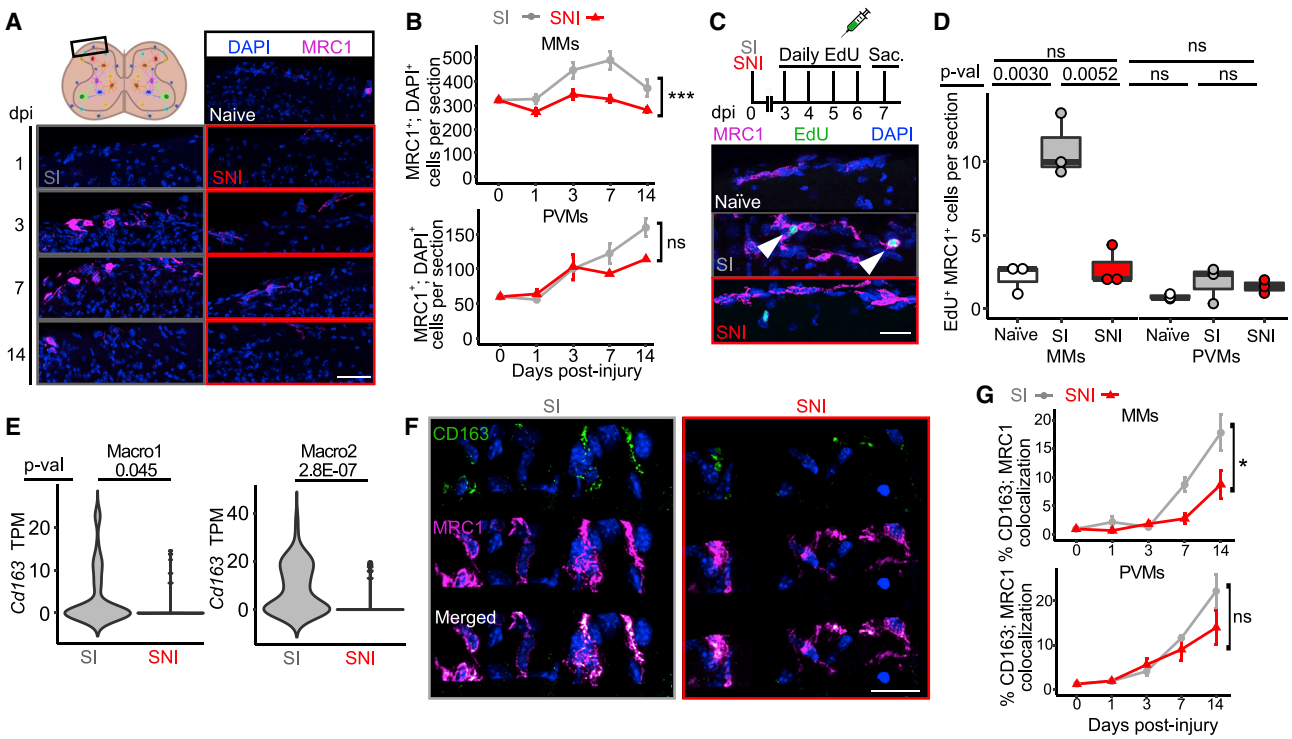

Figure 2. Activation of spinal macrophages is blunted in nerve-injured animals

(A) Representative images of MMs from SI and SNI animals at baseline and 1, 3, 7, and 14 dpi (top scale bar, 20 μm; bottom scale bar, 30 μm; see Figure S3E for representative PVM images over time).

(B) Quantification of the number of MMs and PVMs over time after SI or SNI. n = 3 animals per time point per condition averaging multiple sections per animal (n = 2–6; see STAR methods). Mean ± SEM. (Top) MM: two-way ANOVA. Time point effect: F(4, 24) = 5.638, p = 0.0033. Injury effect (***): F(1, 24) = 20.268, p = 0.00022; Tukey post hoc, 81.78 ± 41.07 fewer MMs per section after SNI. (Bottom) PVM: two-way ANOVA. Time point effect: F(4, 24) = 14.0, p = 1.3E-05. Injury effect: F(1, 24) = 2.573, p = 0.12. See Figure S3F for comparisons between injured and naive animals.

(C) Top: schematic of EdU labeling experiment. Bottom: representative images of EdU-injected naive, SI, and SNI animals (scale bar, 15 μm). Arrowheads, EdU$^+$ MMs.

(D) Quantification of EdU$^+$ MMs and PVMs per section. n = 3 animals per time point per condition averaging multiple sections per animal (n = 2–4; see STAR methods). p values, two-sided Student's t tests. Consecutive datapoints within 1/30th of the range are binned.

(E) *Cd163* expression in Macro1 (SI n = 68, SNI n = 37) and Macro2 (SI n = 66, SNI n = 31) cells from SI and SNI animals. TPM, transcripts per million. p values, binomial test.

(F) CD163 immunostaining of MMs from SI and SNI animals at 14 dpi. Scale bar, 20 μm.

(G) Quantification of CD163 immunostaining in MMs and PVMs over time. n = 3 animals per time point across all conditions averaging multiple sections per animal (n = 2–4; see STAR methods). Mean ± SEM. (Top) MM: two-way ANOVA. Time point effect: F(4, 24) = 18.51, p = 1.7E-06. Injury effect (**): F(1, 24) = 8.64, p = 0.0081; Tukey post hoc, 3.2% ± 2.6% less CD163/MRC1 colocalization after SNI. (Bottom) PVM: two-way ANOVA. Time point effect: F(4, 24) = 16.295, p = 1.41E-06. Injury effect: F(1,24) = 1.422, p = 0.24. See Figure S3I for CD163 expression comparisons between injured and naive animals.

laterality in macrophage populations apart from PVMs in SNI animals, which were more abundant ipsilateral to the side of injury at 14 dpi (Figure S3G). These longitudinal data suggest that spinal macrophage populations expand following a superficial tissue injury and that MM expansion is blunted when the nearby nerve is also injured.

We next injected SI and SNI animals with the thymidine analog 5-ethynyl-2′-deoxyuridine (EdU) to measure the number of MMs and PVMs that entered S phase 3–6 dpi (Figure 2C). Proliferation of MMs, assessed by EdU incorporation, was increased in SI animals relative to naive controls and relative to SNI animals (Figures 2C and 2D). In contrast, EdU labeling of PVMs was not significantly different among naive, SI, and SNI animals (Figure 2D). Together, these findings suggest that a superficial tissue injury promotes expansion of MMs, such as through proliferation and/or migration, and that this expansion is blunted in nerve-injured animals.

Transcriptional responses in spinal macrophages following injury

Hundreds of genes are differentially expressed in bulk spinal cord tissue following peripheral nerve injury (Griffin et al., 2007; Lacroix-Fralish et al., 2006b; Uttam et al., 2018), but these bulk RNA sequencing studies cannot reliably attribute gene expression changes to specific cell types. We thus performed differential gene expression analyses across all 66 cell types, comparing SI with SNI. We detected differentially expressed genes across most of the spinal cell types (a complete list of differentially expressed genes is provided in Table S2). We then used functional Gene Ontology (GO) analyses to gain further insights into how

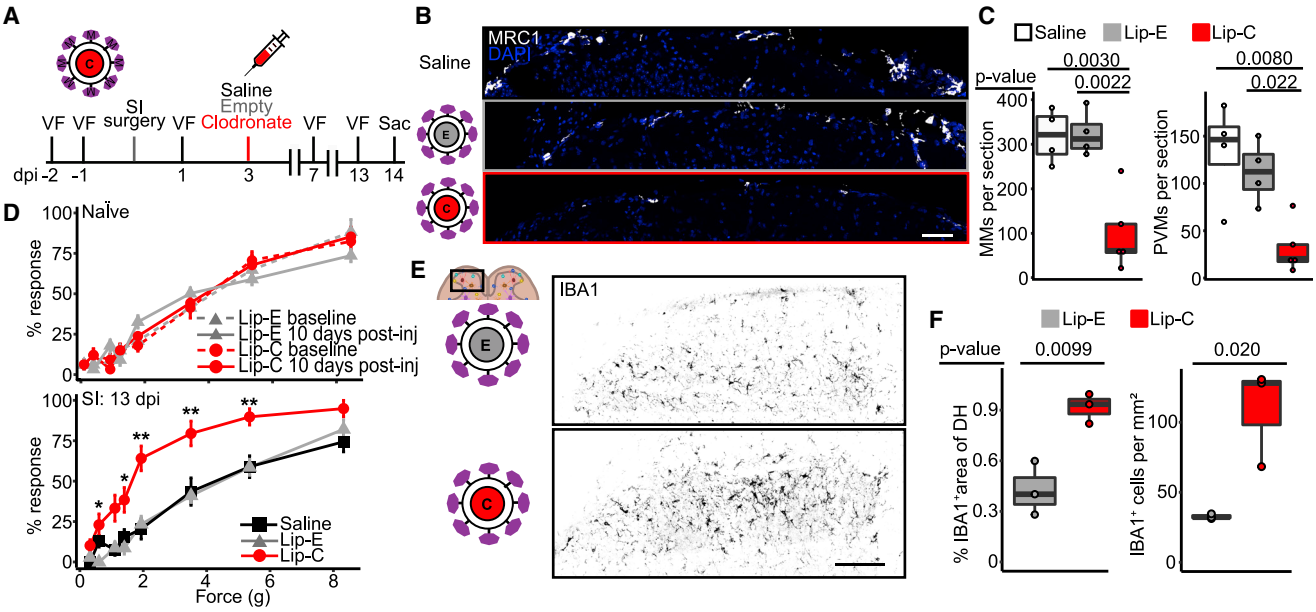

Figure 3. Depletion of MRC1$^+$ spinal macrophage causes persistent mechanical hypersensitivity and microgliosis in SI animals

(A) Experimental outline.

(B) Representative images of MMs and PVMs 11 days post-injection of saline, Lip-E, or Lip-C. Scale bar, 50 μm.

(C) Quantification of MMs and PVMs 11 days post-injection. n = 4, 4, and 5 saline-, Lip-E-, and Lip-C-injected animals, respectively. p values, two-sided Student's t tests. Consecutive datapoints within 1/30th of the range are binned.

(D) Top: mechanical sensitivity in naive animals at baseline and 10 days after Lip-E or Lip-C administration. n = 7 animals per condition. Bottom: mechanical sensitivity 13 dpi in SI animals after saline, Lip-E, or Lip-C administration. n = 7, 8, and 8 animals from saline-, Lip-E-, and Lip-C-treated animals, respectively. Mean ± SEM. Bonferroni-Holm-corrected two-sided Student's t tests between Lip-C and Lip-E animals. *p < 0.05 and **p < 0.01.

(E and F) Representative images of IBA1 expression 14 dpi following Lip-E or Lip-C administration (scale bar, 100 μm) (E) and (F) quantification. IBA1 area and number of IBA1$^+$ cells per dorsal horn. n = 3 animals per condition averaging multiple sections per animal (n = 2–4; see STAR methods). p values, two-sided Student's t test. Consecutive datapoints within 1/30th of the range are binned. DH, dorsal horn.

spinal macrophages responded following nerve injury. None of the upregulated genes in Macro1 or Macro2 cells from SNI animals were associated with a consistent set of pathways. However, many of the downregulated genes in Macro1 and Macro2 cells were associated with cell cycle and proliferation GO terms, consistent with our histological and EdU labeling data above (Figure S3H; complete GO results for Macro1 and Macro2 are provided in Table S3).

Additionally, genes associated with immunoregulatory pathways were reduced in Macro1 and Macro2 cells from SNI animals, including *Jak1*, *Stat3*, and various interleukins (Figure S3H; Table S3). *Cd163*, which encodes a hemoglobin-haptoglobin scavenger receptor that marks anti-inflammatory macrophages and attenuates pro-inflammatory responses (Kim et al., 2006; Philippidis et al., 2004; Yang et al., 2016), was also reduced in Macro1 and Macro2 cells from SNI animals relative to SI controls (Figure 2E). We next histologically quantified CD163/MRC1 colocalization in MMs and PVMs over time. CD163 expression increased over time in both MMs and PVMs, whereas SNI blunted CD163 expression only in MMs (Figures 2F and 2G). Pairwise Tukey post hoc testing revealed that CD163/MRC1 colocalization in MMs increased only in SI animals at 14 dpi compared with baseline levels, whereas colocalization in PVMs increased from baseline at 14 dpi in both injury conditions (Figures S3I). Similar to macrophage expansion, CD163 upregulation was not enriched on either side of the spinal cord (14 dpi data; Figure S3J). Collectively, these data suggest that CD163 is upregulated in MRC1$^+$ spinal macrophages following a superficial injury and that expression of this anti-inflammatory mediator is blunted in MMs when the injury includes the peripheral nerve.

Spinal macrophage depletion leads to persistent pain and microgliosis

In SI animals, proliferation and elevated levels of CD163 temporally coincided with resolution of mechanical hypersensitivity (Figure S1A). Therefore, we hypothesized that MRC1$^+$ spinal macrophages might facilitate the resolution of mechanical hypersensitivity. To test this, we depleted MRC1$^+$ spinal macrophages in SI animals and measured changes in mechanical sensitivity (Figure 3A). Selective depletion was achieved by intrathecally injecting mannosylated liposomes containing clodronate (Lip-C), which binds to MRC1 and induces apoptosis when endocytosed (Van Rooijen and Sanders, 1994). We verified that mannosylated liposomes selectively targeted MRC1$^+$ spinal macrophages when loaded with the fluorescent molecule DiI (Lip-DiI; Figures S4A–S4C; note the absence of DiI in spinal microglia labeled with IBA1 and peripheral macrophages of the DRG). Animals intrathecally injected with Lip-C had fewer MMs and PVMs compared with empty liposomes (Lip-E) and saline control animals (Figures 3B and 3C). Lip-E and Lip-C

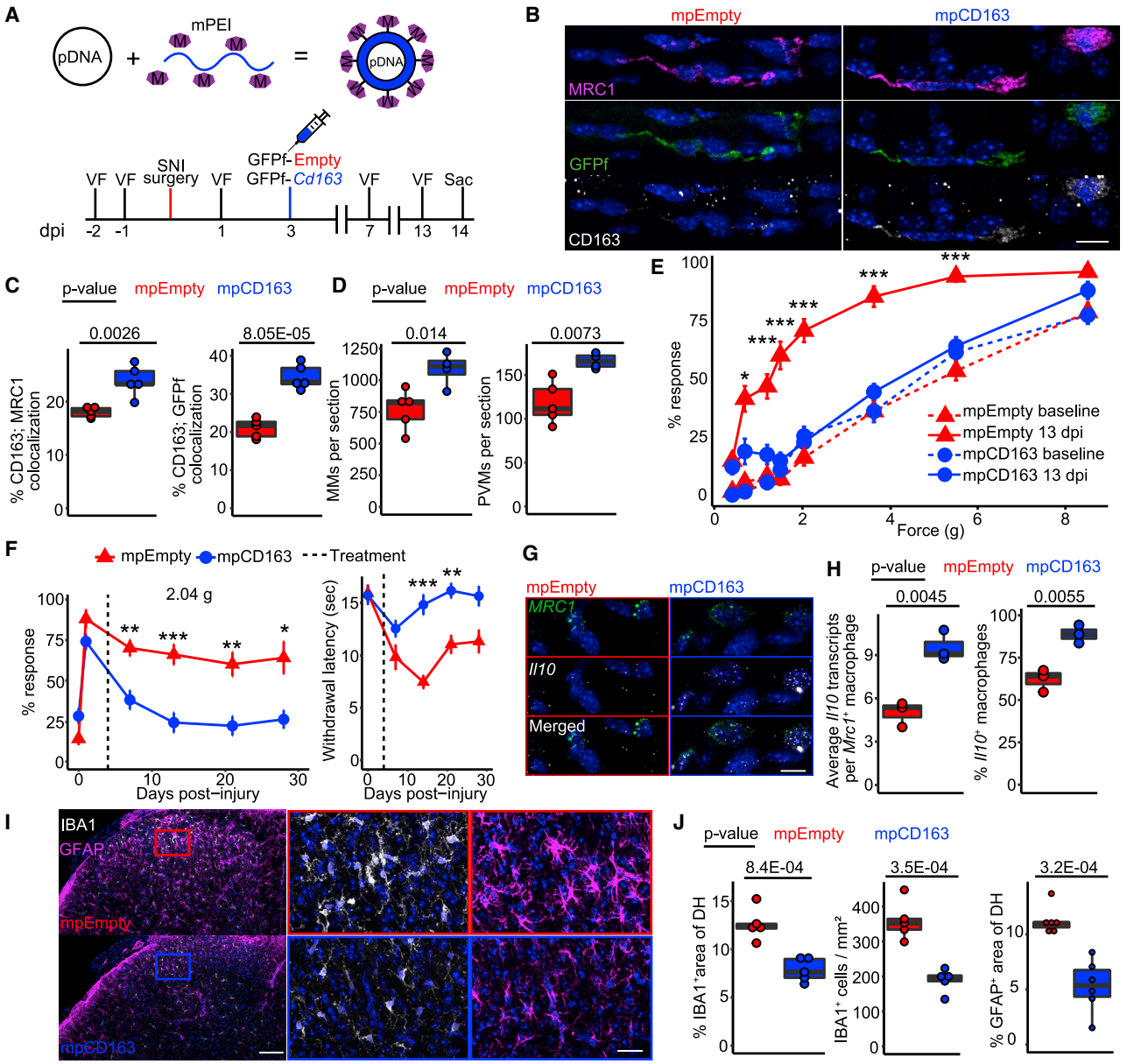

Figure 4. Targeted CD163 expression in MRC1$^+$ spinal macrophages resolves mechanical hypersensitivity, microgliosis, and astrogliosis in SNI animals

(A) Experimental outline.

(B and C) Representative images of GFPf and CD163 colocalization with MRC1 in MMs transfected with mpEmpty or mpCD163 on day 11 post-injection (B), which is 14 dpi (scale bar, 15 μm; see Figure S5A for transfection specificity) and (C) quantification. n = 5 animals per condition averaging two sections per animal. p values, two-sided Student's t tests. Consecutive datapoints within 1/30th of the range are binned.

(D) Quantification of MMs and PVMs 14 dpi after mpEmpty and mpCD163 treatment. n = 5 and 4 animals per condition from mpEmpty- and mpCD163-treated animals, respectively, averaging two or three sections per animal (see STAR methods). p values, two-sided Student's t tests. Consecutive datapoints within 1/30th of the range are binned. See Figure S5E for additional cohort data.

(E) Mechanical sensitivity at baseline and 13 dpi following mpEmpty or mpCD163 treatment. n = 5 animals per condition. Mean ± SEM. Bonferroni-Holm-corrected two-sided Student's t tests between mpCD163 and mpEmpty animals at 13 dpi. *p < 0.05 and ***p < 0.001. See Figure S5D for additional cohort data.

(F) Left: mechanical sensitivity for SNI animals following mpEmpty or mpCD163 treatment at baseline and 1, 3, 7, 14, 21, and 28 dpi. Right: thermal sensitivity measured by Hargreaves assay at baseline and 7, 14, 21, and 28 dpi. n = 10 animals per condition. Mean ± SEM. Bonferroni-Holm-corrected two-sided Student's t tests. *p < 0.05 and ***p < 0.001.

(G) Representative *in situ* hybridization images using *Mrc1* and *Il10* probes in SNI animals following mpEmpty or mpCD163 treatment at 7 dpi. Scale bar, 10 μm.

(legend continued on next page)

administration had no effect on pain thresholds in naive (uninjured) animals (Figure 3D). In contrast, Lip-C-treated SI animals showed profound mechanical hypersensitivity relative to controls (Lip-E or saline injected; Figure 3D). Moreover, Lip-C-treated SI animals exhibited signs of microglial activation, as evidenced by an increase in the total area of spinal IBA1 and the number of IBA1$^+$ cells (Figures 3E and 3F; relative to Lip-E controls). Microglial activation is a hallmark feature of peripheral nerve injury (Echeverry et al., 2017; Eriksson et al., 1993), which we reproduced (Figure S4D). Together, these data indicate that pain fails to resolve in SI animals when MRC1$^+$ spinal macrophages are depleted. Moreover, these findings suggest that the pro- and anti-inflammatory balance between microglia and spinal macrophages, respectively, is dysregulated following nerve injury (Figure S4E).

Increasing CD163 expression in spinal macrophages resolves neuroinflammation and neuropathic pain

As spinal macrophages proliferate, upregulate *Cd163*, and are required for pain resolution in SI animals, we hypothesized that polarizing spinal macrophages toward an anti-inflammatory state in SNI animals might resolve persistent neuroinflammation and mechanical hypersensitivity. To polarize MRC1$^+$ spinal macrophages *in vivo*, we intrathecally injected mice with mannosylated polyethylenimine nanoparticles (mPEIs) loaded with a mouse *Cd163* expression plasmid. Control mPEIs were loaded with an empty expression vector. Experimental and control mPEIs were co-complexed with a farnesylated GFP (GFPf) plasmid to identify transfected cells. Similar to Lip-DiI, GFP transfection was restricted to MRC1$^+$ spinal macrophages (Figure S5A). This mPEI formulation was chosen because (1) mannose-conjugated nanoparticles target MRC1-expressing spinal macrophages (above), (2) CD163 signaling induces anti-inflammatory IL-10 production and secretion (Philippidis et al., 2004; Yang et al., 2016), (3) expression of CD163 decreases pro-inflammatory cytokine expression in lipopolysaccharide-stimulated human primary macrophages (Alvarado-Vazquez et al., 2017), and (4) CD163 can positively regulate cell proliferation (Chen et al., 2019).

We intrathecally injected SNI animals with mPEI-GFPf-CD163 (mpCD163) or mPEI-GFPf-empty vector (mpEmpty) at 4 dpi (Figure 4A). SNI animals treated with mpCD163 had higher CD163 expression in MRC1$^+$ spinal macrophages 14 dpi compared with mpEmpty-treated controls (Figures 4B, 4C, and S5B). Additionally, CD163 expression resulted in an expansion of MM and PVM populations (Figure 4D). Although mpEmpty and mpCD163 had no effect on mechanical sensitivity in naive animals (Figure S5C), mpCD163 treatment decreased mechanical sensitivity in SNI animals 13 dpi compared with mpEmpty controls (Figure 4E). The attenuation of mechanical sensitivity began by 7 dpi (3 days post-treatment) and persisted through 28 dpi (Figure 4F). Moreover, mpCD163 treatment alleviated thermal hypersensitivity by 13 dpi compared with mpEmpty controls (Figure 4F). To confirm anti-inflammatory polarization in spinal macrophages, we performed *in situ* hybridization to probe for the anti-inflammatory cytokine interleukin-10 (*Il10*). Treatment with mpCD163 increased the number of *Il10* transcripts in *Mrc1*$^+$ cells and increased the proportion of *Il10*$^+$; *Mrc1*$^+$ macrophages by 7 dpi (3 days post-treatment; Figures 4G and 4H). Consistent with anti-inflammatory polarization, IBA1 area, IBA1$^+$ cell number, and glial fibrillary acidic protein (GFAP; an astrocyte marker) area were reduced in mpCD163-treated animals (Figures 4I and 4J). We independently replicated the behavioral and neuroimmune effects of targeted mpCD163 treatment in a separate cohort of animals (Figures S5D–S5F). Note that these effects on behavior were dosage dependent, as injecting mice with a higher amount of mpCD163 resulted in an abnormal expansion of MRC1$^+$ macrophages, as predicted (Chen et al., 2019), but no statistically significant change (increase or decrease) in mechanical sensitivity in SNI animals (Figure S5G). Together, these data suggest that targeted elevation of CD163 in MRC1$^+$ spinal macrophages of neuropathic animals can resolve neuroinflammation and attenuate mechanical hypersensitivity.

DISCUSSION

The spinal neuroimmune response following nerve injury has traditionally been viewed as unidirectional (pro-inflammatory) (Inoue and Tsuda, 2018), though the cells involved in this response can be coaxed to exhibit anti-inflammatory properties (Chen et al., 2018). Our data suggest a more complex relationship whereby microglia, and possibly other cell types including astrocytes (Figure 4J), are actively restrained by anti-inflammatory spinal MRC1$^+$ macrophages following superficial injury, and this active restraint fails in a pathological nerve injury condition (Figure S4E).

The concept that resident macrophages can activate and resolve inflammation in other regions of the body is not new (Bedoret et al., 2009; McGaha et al., 2011; Miyake et al., 2007; Pinto et al., 2012; Serrats et al., 2010; Winnall et al., 2011). However, this concept has never been explored in the spinal cord in the context of neuropathic pain. Our discovery stems, in part, from a methodological difference in terms of how spinal cells are studied following a nerve injury. It is common for labs to examine the contralateral spinal cord of nerve-injured animals as a control or to compare responses in nerve-injured animals days to weeks after the nerve injury versus sham controls that are either not injured at all or are superficially injured (but examined at a time post-injury that differs from the experimental group). Our data show that MRC1$^+$ macrophages are, in fact, activated in nerve-injured animals (increased number and CD163 expression), but what was unexpected is that this

(H) Quantification of the mean number of *Il10* transcripts in *Mrc1*$^+$ cells (left) and of the mean proportion of *Mrc1*$^+$ macrophages expressing >3 *Il10* transcripts (right) from SNI animals after mpEmpty or mpCD163 treatment 7 dpi. n = 3 animals per condition averaging two sections per animal. p values, two-sided Student's t tests. Consecutive datapoints within 1/30th of the range are binned.

(I and J) Representative images of IBA1 and GFAP expression from mpEmpty- and mpCD163-treated SNI animals 14 dpi (I) (left scale bar, 100 μm; right scale bar, 20 μm) and (J) quantification of IBA1 area, IBA1$^+$ cells, and GFAP area. n = 5, 5, and 6 animals per condition for IBA1 area, IBA1 cells, and GFAP area, respectively. IBA1 datapoints generated from averaging two sections per animal. p values, two-sided Student's t tests. Consecutive datapoints within 1/30th of the range are binned. DH, dorsal horn. See Figure S5F for additional cohort data.

activation response was blunted relative to the SI animals. This blunted activation process would have been overlooked or misclassified had we instead drawn comparisons with naive mice or with the contralateral spinal cord. The mechanisms that prevent spinal MRC1$^+$ macrophages from being fully activated in nerve-injured animals are unknown and will require further study. However, spinal macrophages in nerve-injured animals are not permanently disabled, as targeted expression of *Cd163*, an anti-inflammatory mediator that MRC1$^+$ macrophages endogenously upregulate in SI animals, increased spinal macrophage *Il10* production, limited micro- and astrogliosis, and enduringly resolved neuropathic pain. Our data also point to the importance of increasing CD163 to a level that approximates that of SI animals, as non-physiological levels of CD163 stimulated excessive proliferation/expansion of spinal macrophages and had no effect on pain resolution. We speculate the failure of high-dose CD163 to resolve hypersensitivity may be related to the abnormally large number of MMs in the meningeal space, possibly impeding and/or counteracting MM function.

A variety of pathological pain conditions are associated with neuroinflammation in the spinal cord. Moreover, activated macrophages in the dorsal root ganglia were recently implicated in the initiation and persistence of neuropathic pain (Yu et al., 2020). However, the experimental approaches used in this study non-selectively ablated all resident macrophage subtypes and almost 90% of all mature circulating monocytes. Macrophages that upregulate anti-inflammatory mediators, such as *Cd163*, would presumably have been ablated as well, which we predict would obscure or eliminate any potential anti-inflammatory macrophage response in the DRG. Although our functional approaches showed greater cell type specificity, we cannot rule out a potential contribution of MRC1$^+$ macrophages in the dorsal roots proximal to the spinal cord, which were also labeled by mannosylated liposomes/nanoparticles (Figures S4B and S5A). Other neuropathic pain models (chronic constriction injury and spinal nerve ligation) (Colburn et al., 1997; Hua et al., 2005) and inflammatory pain models (formalin and carrageenan) (Fu et al., 1999; Hua et al., 2005) induce neuroinflammation in the spinal cord, but whether an opposing anti-inflammatory response in spinal macrophages is present is unknown. Our work has the potential to stimulate further study of anti-inflammatory macrophage responses and the extent to which these responses are dampened in other pathological pain conditions.

Pro-inflammatory spinal microglia are activated in males and females following peripheral nerve injury, and it is increasingly recognized that inflammatory contributions to neuropathic pain differ between males and females (Brings and Zylka, 2015; LaCroix-Fralish et al., 2006a; Sorge et al., 2015). We acknowledge that our experiments were carried out in male animals, and that extensive future experimental work will be needed to evaluate the extent to which anti-inflammatory MRC1$^+$ spinal macrophages participate in pain resolution in females and if these macrophages act via similar or distinct mechanisms.

STAR★METHODS

Detailed methods are provided in the online version of this paper and include the following:

SUPPLEMENTAL INFORMATION

Supplemental Information can be found online at https://doi.org/10.1016/j.neuron.2021.02.018.

ACKNOWLEDGMENTS

This research was supported by the National Institute of Neurological Disorders and Stroke (NINDS; grants R21NS106337 and R01NS114259 to M.J.Z., grants F31NS105397 and T32NS007431 to J.K.N., and grant P30NS045892 to J.M.S.) and the Eunice Kennedy Shriver National Institute of Child Health and Human Development (NICHD; grant U54HD079124 to J.M.S.). Sequencing was performed at the University of North Carolina (UNC) High Throughput Sequencing Core. Microscopy was performed at the UNC Neuroscience Center Microscopy Core, supported by the NINDS (grant P30NS045892) and the NICHD (grant U54HD079124).

AUTHOR CONTRIBUTIONS

J.K.N. and M.J.Z. designed the study. B.T.-B. assisted with histological experiments. L.L. flowed cells on Drop-seq days and provided scRNA-seq advice. J.M.S. established Drop-seq demultiplexing and alignment pipeline and provided scRNA-seq advice. J.K.N. performed experiments and bioinformatic analyses. J.K.N. and M.J.Z. wrote the manuscript.

DECLARATION OF INTERESTS

The authors declare no competing interests.

Received: July 8, 2019
Revised: September 28, 2020
Accepted: February 12, 2021
Published: March 4, 2021

REFERENCES

Albrecht, D.S., Ahmed, S.U., Kettner, N.W., Borra, R.J.H., Cohen-Adad, J., Deng, H., Houle, T.T., Opalacz, A., Roth, S.A., Melo, M.F.V., et al. (2018). Neuroinflammation of the spinal cord and nerve roots in chronic radicular pain patients. Pain *159*, 968–977.

Alles, J., Karaiskos, N., Praktiknjo, S.D., Grosswendt, S., Wahle, P., Ruffault, P.L., Ayoub, S., Schreyer, L., Boltengagen, A., Birchmeier, C., et al. (2017).

Cell fixation and preservation for droplet-based single-cell transcriptomics. BMC Biol. *15*, 44.

Alvarado-Vazquez, P.A., Bernal, L., Paige, C.A., Grosick, R.L., Moracho Vilrriales, C., Ferreira, D.W., Ulecia-Morón, C., and Romero-Sandoval, E.A. (2017). Macrophage-specific nanotechnology-driven CD163 overexpression in human macrophages results in an M2 phenotype under inflammatory conditions. Immunobiology *222*, 900–912.

Bedoret, D., Wallemacq, H., Marichal, T., Desmet, C., Quesada Calvo, F., Henry, E., Closset, R., Dewals, B., Thielen, C., Gustin, P., et al. (2009). Lung interstitial macrophages alter dendritic cell functions to prevent airway allergy in mice. J. Clin. Invest. *119*, 3723–3738.

Bennett, Mariko L., Bennett, F. Chris, Liddelow, Shane A., Ajami, Bahareh, Zamanian, Jennifer L., Fernhoff, Nathaniel B., Mulinyawe, Sara B., Bohlen, Christopher J., Adil, Aykezar, Tucker, Andrew, et al. (2016). New tools for studying microglia in the mouse and human CNS. PNAS. https://doi.org/10.1073/pnas.1525528113.

Brings, V.E., and Zylka, M.J. (2015). Sex, drugs and pain control. Nat. Neurosci. *18*, 1059–1060.

Chen, G., Zhang, Y.Q., Qadri, Y.J., Serhan, C.N., and Ji, R.R. (2018). Microglia in pain: detrimental and protective roles in pathogenesis and resolution of pain. Neuron *100*, 1292–1311.

Chen, Jing, Bardes, Eric E., Aronow, Bruce J., and Jegga, Anil G. (2009). ToppGene Suite for gene list enrichment analysis and candidate gene prioritization. Nucleic Acids Research. https://doi.org/10.1093/nar/gkp427.

Chen, T., Chen, J., Zhu, Y., Li, Y., Wang, Y., Chen, H., Wang, J., Li, X., Liu, Y., Li, B., et al. (2019). CD163, a novel therapeutic target, regulates the proliferation and stemness of glioma cells via casein kinase 2. Oncogene *38*, 1183–1199.

Colburn, R.W., DeLeo, J.A., Rickman, A.J., Yeager, M.P., Kwon, P., and Hickey, W.F. (1997). Dissociation of microglial activation and neuropathic pain behaviors following peripheral nerve injury in the rat. J. Neuroimmunol. *79*, 163–175.

Costigan, M., Scholz, J., and Woolf, C.J. (2009). Neuropathic pain: a maladaptive response of the nervous system to damage. Annu. Rev. Neurosci. *32*, 1–32.

Dobin, A., Davis, C.A., Schlesinger, F., Drenkow, J., Zaleski, C., Jha, S., Batut, P., Chaisson, M., and Gingeras, T.R. (2013). STAR: ultrafast universal RNA-seq aligner. Bioinformatics *29*, 15–21.

Echeverry, S., Shi, X.Q., Yang, M., Huang, H., Wu, Y., Lorenzo, L.E., Perez-Sanchez, J., Bonin, R.P., De Koninck, Y., and Zhang, J. (2017). Spinal microglia are required for long-term maintenance of neuropathic pain. Pain *158*, 1792–1801.

Eisenach, J.C., Curry, R., Tong, C., Houle, T.T., and Yaksh, T.L. (2010). Effects of intrathecal ketorolac on human experimental pain. Anesthesiology *112*, 1216–1224.

Eriksson, N.P., Persson, J.K., Svensson, M., Arvidsson, J., Molander, C., and Aldskogius, H. (1993). A quantitative analysis of the microglial cell reaction in central primary sensory projection territories following peripheral nerve injury in the adult rat. Exp. Brain Res. *96*, 19–27.

Fu, K.Y., Light, A.R., Matsushima, G.K., and Maixner, W. (1999). Microglial reactions after subcutaneous formalin injection into the rat hind paw. Brain Res. *825*, 59–67.

Goldmann, T., Wieghofer, P., Jordão, M.J., Prutek, F., Hagemeyer, N., Frenzel, K., Amann, L., Staszewski, O., Kierdorf, K., Krueger, M., et al. (2016). Origin, fate and dynamics of macrophages at central nervous system interfaces. Nat. Immunol. *17*, 797–805.

Griffin, R.S., Costigan, M., Brenner, G.J., Ma, C.H., Scholz, J., Moss, A., Allchorne, A.J., Stahl, G.L., and Woolf, C.J. (2007). Complement induction in spinal cord microglia results in anaphylatoxin C5a-mediated pain hypersensitivity. J. Neurosci. *27*, 8699–8708.

Hargreaves, K., Dubner, R., Brown, F., Flores, C., and Joris, J. (1988). A new and sensitive method for measuring thermal nociception in cutaneous hyperalgesia. Pain *32*, 77–88.

Häring, M., Zeisel, A., Hochgerner, H., Rinwa, P., Jakobsson, J.E.T., Lönnerberg, P., La Manno, G., Sharma, N., Borgius, L., Kiehn, O., et al. (2018). Neuronal atlas of the dorsal horn defines its architecture and links sensory input to transcriptional cell types. Nat. Neurosci. *21*, 869–880.

Hua, X.Y., Svensson, C.I., Matsui, T., Fitzsimmons, B., Yaksh, T.L., and Webb, M. (2005). Intrathecal minocycline attenuates peripheral inflammation-induced hyperalgesia by inhibiting p38 MAPK in spinal microglia. Eur. J. Neurosci. *22*, 2431–2440.

Inoue, K., and Tsuda, M. (2018). Microglia in neuropathic pain: cellular and molecular mechanisms and therapeutic potential. Nat. Rev. Neurosci. *19*, 138–152.

Johnson, W. Evan, Li, Cheng, and Rabinovic, Ariel (2007). Adjusting batch effects in microarray expression data using empirical Bayes methods. Biostatistics *8* (1), https://doi.org/10.1093/biostatistics/kxj037.

Jordão, M.J.C., Sankowski, R., Brendecke, S.M., Sagar, Locatelli, G., Tai, Y.H., Tay, T.L., Schramm, E., Armbruster, S., Hagemeyer, N., et al. (2019). Single-cell profiling identifies myeloid cell subsets with distinct fates during neuroinflammation. Science *363*, eaat7554.

Kim, W.K., Alvarez, X., Fisher, J., Bronfin, B., Westmoreland, S., McLaurin, J., and Williams, K. (2006). CD163 identifies perivascular macrophages in normal and viral encephalitic brains and potential precursors to perivascular macrophages in blood. Am. J. Pathol. *168*, 822–834.

Konishi, Hiroyuki, Kobayashi, Masaaki, Kunisawa, Taikan, Imai, Kenta, Sayo, Akira, Malissen, Bernard, Crocker, Paul R., Sato, Katsuaki, and Kiyama, Hiroshi (2017). Siglec-H is a microglia-specific marker that discriminates microglia from CNS-associated macrophages and CNS-infiltrating monocytes. Glia. https://doi.org/10.1002/glia.23204.

LaCroix-Fralish, M.L., Tawfik, V.L., Spratt, K.F., and DeLeo, J.A. (2006a). Sex differences in lumbar spinal cord gene expression following experimental lumbar radiculopathy. J. Mol. Neurosci. *30*, 283–295.

Lacroix-Fralish, M.L., Tawfik, V.L., Tanga, F.Y., Spratt, K.F., and DeLeo, J.A. (2006b). Differential spinal cord gene expression in rodent models of radicular and neuropathic pain. Anesthesiology *104*, 1283–1292.

Loo, L., Simon, J.M., Xing, L., McCoy, E.S., Niehaus, J.K., Guo, J., Anton, E.S., and Zylka, M.J. (2019). Single-cell transcriptomic analysis of mouse neocortical development. Nat. Commun. *10*, 134.

Macosko, Evan Z., Basu, Anindita, Satija, Rahul, Nemesh, James, Shekhar, Karthik, Goldman, Melissa, Tirosh, Itay, Bialas, Allison R., Kamitaki, Nolan, Martersteck, Emily M., et al. (2015). Highly Parallel Genome-wide Expression Profiling of Individual Cells Using Nanoliter Droplets. Cell. https://doi.org/10.1016/j.cell.2015.05.002.

McGaha, T.L., Chen, Y., Ravishankar, B., van Rooijen, N., and Karlsson, M.C. (2011). Marginal zone macrophages suppress innate and adaptive immunity to apoptotic cells in the spleen. Blood *117*, 5403–5412.

Miyake, Y., Asano, K., Kaise, H., Uemura, M., Nakayama, M., and Tanaka, M. (2007). Critical role of macrophages in the marginal zone in the suppression of immune responses to apoptotic cell-associated antigens. J. Clin. Invest. *117*, 2268–2278.

Ostenfeld, T., Krishen, A., Lai, R.Y., Bullman, J., Green, J., Anand, P., Scholz, J., and Kelly, M. (2015). A randomized, placebo-controlled trial of the analgesic efficacy and safety of the p38 MAP kinase inhibitor, losmapimod, in patients with neuropathic pain from lumbosacral radiculopathy. Clin. J. Pain *31*, 283–293.

Philippidis, P., Mason, J.C., Evans, B.J., Nadra, I., Taylor, K.M., Haskard, D.O., and Landis, R.C. (2004). Hemoglobin scavenger receptor CD163 mediates interleukin-10 release and heme oxygenase-1 synthesis: antiinflammatory monocyte-macrophage responses in vitro, in resolving skin blisters in vivo, and after cardiopulmonary bypass surgery. Circ. Res. *94*, 119–126.

Pinto, A.R., Paolicelli, R., Salimova, E., Gospocic, J., Slonimsky, E., Bilbao-Cortes, D., Godwin, J.W., and Rosenthal, N.A. (2012). An abundant tissue macrophage population in the adult murine heart with a distinct alternatively-activated macrophage profile. PLoS ONE *7*, e36814.

Ruan, C., Sun, L., Kroshilina, A., Beckers, L., De Jager, P., Bradshaw, E.M., Hasson, S.A., Yang, G., and Elyaman, W. (2020). A novel Tmem119-tdTomato reporter mouse model for studying microglia in the central nervous system. Brain Behav. Immun. *83*, 180–191.

Sathyamurthy, A., Johnson, K.R., Matson, K.J.E., Dobrott, C.I., Li, L., Ryba, A.R., Bergman, T.B., Kelly, M.C., Kelley, M.W., and Levine, A.J. (2018). Massively parallel single nucleus transcriptional profiling defines spinal cord neurons and their activity during behavior. Cell Rep. *22*, 2216–2225.

Schindelin, J., Arganda-Carreras, I., Frise, E., Kaynig, V., Longair, M., Pietzsch, T., Preibisch, S., Rueden, C., Saalfeld, S., Schmid, B., et al. (2012). Fiji: an open-source platform for biological-image analysis. Nat. Methods *9*, 676–682.

Serrats, J., Schiltz, J.C., García-Bueno, B., van Rooijen, N., Reyes, T.M., and Sawchenko, P.E. (2010). Dual roles for perivascular macrophages in immune-to-brain signaling. Neuron *65*, 94–106.

Shekhar, K., Lapan, S.W., Whitney, I.E., Tran, N.M., Macosko, E.Z., Kowalczyk, M., Adiconis, X., Levin, J.Z., Nemesh, J., Goldman, M., et al. (2016). Comprehensive classification of retinal bipolar neurons by single-cell transcriptomics. Cell *166*, 1308–1323.e30.

Shields, S.D., Eckert, W.A., 3rd, and Basbaum, A.I. (2003). Spared nerve injury model of neuropathic pain in the mouse: a behavioral and anatomic analysis. J. Pain *4*, 465–470.

Sorge, R.E., Mapplebeck, J.C., Rosen, S., Beggs, S., Taves, S., Alexander, J.K., Martin, L.J., Austin, J.S., Sotocinal, S.G., Chen, D., et al. (2015). Different immune cells mediate mechanical pain hypersensitivity in male and female mice. Nat. Neurosci. *18*, 1081–1083.

Stratton, J.A., Holmes, A., Rosin, N.L., Sinha, S., Vohra, M., Burma, N.E., Trang, T., Midha, R., and Biernaskie, J. (2018). Macrophages regulate schwann cell maturation after nerve injury. Cell Rep. *24*, 2561–2572.e6.

Ting, J.T., Daigle, T.L., Chen, Q., and Feng, G. (2014). Acute brain slice methods for adult and aging animals: application of targeted patch clamp analysis and optogenetics. Methods Mol. Biol. *1183*, 221–242.

Uttam, S., Wong, C., Amorim, I.S., Jafarnejad, S.M., Tansley, S.N., Yang, J., Prager-Khoutorsky, M., Mogil, J.S., Gkogkas, C.G., and Khoutorsky, A. (2018). Translational profiling of dorsal root ganglia and spinal cord in a mouse model of neuropathic pain. Neurobiol. Pain *4*, 35–44.

van der Maaten, Laurens, and Hinton, Geoffrey (2008). Journal of Machine Learning Research.

Van Hove, H., Martens, L., Scheyltjens, I., De Vlaminck, K., Pombo Antunes, A.R., De Prijck, S., Vandamme, N., De Schepper, S., Van Isterdael, G., Scott, C.L., et al. (2019). A single-cell atlas of mouse brain macrophages reveals unique transcriptional identities shaped by ontogeny and tissue environment. Nat. Neurosci. *22*, 1021–1035.

Van Rooijen, N., and Sanders, A. (1994). Liposome mediated depletion of macrophages: mechanism of action, preparation of liposomes and applications. J. Immunol. Methods *174*, 83–93.

Vanelderen, P., Van Zundert, J., Kozicz, T., Puylaert, M., De Vooght, P., Mestrum, R., Heylen, R., Roubos, E., and Vissers, K. (2015). Effect of minocycline on lumbar radicular neuropathic pain: a randomized, placebo-controlled, double-blind clinical trial with amitriptyline as a comparator. Anesthesiology *122*, 399–406.

Wang, L., Bauer, M., Curry, R., Larsson, A., Sessler, D.I., and Eisenach, J.C. (2014). Intrathecal ketorolac does not improve acute or chronic pain after hip arthroplasty: a randomized controlled trial. J. Anesth. *28*, 790–793.

Winnall, W.R., Muir, J.A., and Hedger, M.P. (2011). Rat resident testicular macrophages have an alternatively activated phenotype and constitutively produce interleukin-10 in vitro. J. Leukoc. Biol. *90*, 133–143.

Yang, H., Wang, H., Levine, Y.A., Gunasekaran, M.K., Wang, Y., Addorisio, M., Zhu, S., Li, W., Li, J., de Kleijn, D.P., et al. (2016). Identification of CD163 as an antiinflammatory receptor for HMGB1-haptoglobin complexes. JCI Insight *1*, e85375.

Yu, Xiaobing, Liu, Hongju, Hamel, Katherine A., Morvan, Maelig G., Yu, Stephen, Leff, Jacqueline, Guan, Zhonghui, Braz, Joao M., and Basbaum, Allan I. (2020). Dorsal root ganglion macrophages contribute to both the initiation and persistence of neuropathic pain. Nature Communications. https://doi.org/10.1038/s41467-019-13839-2.

Zeisel, A., Hochgerner, H., Lönnerberg, P., Johnsson, A., Memic, F., van der Zwan, J., Häring, M., Braun, E., Borm, L.E., La Manno, G., et al. (2018). Molecular architecture of the mouse nervous system. Cell *174*, 999–1014.e22.

Zhang, J., and De Koninck, Y. (2006). Spatial and temporal relationship between monocyte chemoattractant protein-1 expression and spinal glial activation following peripheral nerve injury. J. Neurochem. *97*, 772–783.

STAR★METHODS

KEY RESOURCE TABLE

REAGENT or RESOURCE	SOURCE	IDENTIFIER
Antibodies		
Rabbit Monoclonal Anti-CD163 (1:200)	Abcam	Cat# ab182422; RRID:AB_2753196
Goat Polyclonal Anti-MRC1/MMR/ CD206 (1:200)	R and D Systems	Cat# AF2535; RRID:AB_2063012
Rabbit Polyclonal Anti-IBA1 (1:400)	WAKO	Cat# 019-19741; RRID:AB_839504
Chicken Polyclonal Anti-GFAP (1:1000)	Novus Biologicals	Cat# NBP1-05198; RRID:AB_1556315
Chicken Polyclonal Anti-GFP (1:2000)	Aves Labs	Cat# GFP-1010; RRID:AB_2307313
Cy3 Donkey Anti-Rat IgG (H+L) (1:500)	Jackson ImmunoResearch Labs	Cat# 712-165-153; RRID:AB_2340667
Alexa Fluor 488 Donkey Anti-Goat IgG (H+L) (1:500)	Jackson ImmunoResearch Labs	Cat# 705-545-147; RRID:AB_2336933
Alexa Fluor 647 Donkey Anti-Rabbit IgG (H+L) (1:500)	Thermo Fisher Scientific	Cat# A-31573; RRID:AB_2536183
Alexa Fluor 488 Goat Anti-Mouse IgG1 (1:500)	Thermo Fisher Scientific	Cat# A-21121; RRID:AB_2535764
Alexa Fluor 568 Goat Anti-Mouse IgG2a (1:500)	Thermo Fisher Scientific	Cat# A-21134; RRID:AB_2535773
Alexa Fluor 633 Goat Anti-Rabbit IgG (H+L) (1:500)	Thermo Fisher Scientific	Cat# A-21070; RRID:AB_2535731
Alexa Fluor 647 Donkey Anti-Chicken IgG (H+L) (1:500)	Jackson ImmunoResearch Labs	Cat# 703-605-155; RRID:AB_2340379
Chemicals, peptides, and recombinant proteins		
Ficoll PM-400	GE Healthcare	Cat# 17030008
Sarkosyl	Sigma	Cat# L7414
UltraPure 0.5 M EDTA, pH 8.0	Thermo Fisher Scientific	Cat# 15575020
UltraPure SDS Solution, 10%	Thermo Fisher Scientific	*Cat# 15553027*
Tris 1 M, pH 8.0	Thermo Fisher Scientific	Cat# AM9856
UltraPure Tris 1 M, pH 7.5	Thermo Fisher Scientific	Cat# 15567027
UltraPure SSC, 20x	Thermo Fisher Scientific	Cat# 15557-044
Barcoded Beads	Chemgenes	Cat# MACOSKO-2011-10
Tween-20	Sigma	Cat# P1379-500ML
Droplet Generation Oil for Evagreen	Bio-Rad	Cat# 1864006
DL-Dithiothreitol Solution 1 M	Sigma	Cat# 43816
Perfluorooctanol	Sigma	Cat# 370533
TrypLE Express Enzyme	Thermo Fisher Scientific	Cat# 12604013
Maxima H Minus Reverse Transcriptase	Thermo Fisher Scientific	Cat# EP0753
Advantage UltraPure PCA dNTPs (10 mM each)	Clontech	Cat# 639125
NxGen RNase Inhibitor	Lucigen	Cat# 30281-2
Exonuclease I (*E. coli*)	New England Biolabs	Cat# M0293S
2x HiFi Hotstart Readymix	Kapa Biosystems	Cat# KK2602
Agencourt Ampure XP beads	Beckman Coulter	Cat# A63880
SYTOX green	Life Technologies	Cat# S7020
Protease from Streptomyces griseus	Sigma	Cat# P5147
Collagenase Type 1 (CLS-1)	Worthington	Cat# LS004196
Percoll	GE Healthcare	Cat# 17-0891-02
Sodium Pyruvate (100 mM)	GIBCO	Cat# 11360070
N-Methyl-D-glucamine	Sigma	Cat# M2004-100G
Tetrodotoxin Citrate	Tocris	Cat# 1069
D-AP5	Abcam	Cat# ab120003

(*Continued on next page*)

Continued

REAGENT or RESOURCE	SOURCE	IDENTIFIER
DNQX disodium salt	Tocris	Cat# 2312
5-ethynyl-2′-deoxyuridine (EdU)	Cayman Chemicals	Cat# 20518
Critical commercial assays		
Agilent High Sensitivity DNA Kit	Agilent Technologies	Cat# 5067-4626
Mannosylated Macrophage Depletion Kit	Encapsula Nano Sciences	Cat# CLD-8914
in vivo-jetPEI-Man	Polyplus Transfection	Cat# 203-10G
Nextera XT DNA Library Preparation Kit	Illumina	Cat# FC-131-1096
RNAscope® Probe- Mm-Mrc1-C3	ACDBio	437511-C3
RNAscope® Probe- Mm-Il10	ACDBio	317261
RNAscope® Fluorescent multiples Detection Reagents	ACDBio	320851
RNAscope® protease III & IV Reagents	ACDBio	322340
RNAscope® Target Retrieval Reagents	ACDBio	322000
Deposited data		
Single-cell RNA sequencing	Gene Expression Omnibus	Accession# GSE134003
Experimental models: cell lines		
HEK293T	ATCC	Cat# CRL-3216; RRID:CVCL_0063
Experimental models: organisms/strains		
Mouse: C57BL/6J	Jackson Laboratory	Cat# JAX:000664; RRID:IMSR_JAX:000664
Oligonucleotides		
Barcoded Bead SeqB: 5′ –Bead–Linker-TTTTTTTAAGCAGTGGTATCAAC GCAGAGTACJJJJJJJJJJJNNNNNNNN TTTTTTTTTTTTTTTTTTTTTTTTTTTTT-3′	Macosko et al., 2015	N/A
TSO: 5′ -AAGCAGTGGTATCAACGCA GAGTGAATrGrGrG −3′	Macosko et al., 2015	N/A
TSO_PCR: 5′ – AAGCAGTGGTAT CAACGCAGAGT −3′	Macosko et al., 2015	N/A
P5-TSO_Hybrid: 5′ - AATGATACGGCGACCACCGAGATC TACACGCCTGTCCGCGGAAGCAGTG GTATCAACGCAGAGT* A*C −3′	Macosko et al., 2015	N/A
Custom Read 1 Primer: 5′ - GCCTGTCCGCGGAAGCAGTGGTATC AACGCAG AGTAC −3′		N/A
Nextera XT Index Kit v2 Set A (96 indexes)	Illumina	Cat# FC-131-2001
Nextera XT Index Kit v2 Set B (96 indexes)	Illumina	Cat# FC-131-2002
Recombinant DNA		
pCD163 (mouse ORF)	Sino Biological	Cat# MG51057-CH
Software and algorithms		
Drop-seq_tools(v1.12)	Macosko et al., 2015	http://mccarrolllab.com/dropseq/; RRID: SCR_018142
Clustering and differential gene expression	Shekhar et al., 2016	https://github.com/broadinstitute/BipolarCell2016
Cluster optimization	Loo et al., 2019	https://github.com/jeremymsimon/MouseCortex
t-distributed stochastic neighbor embedding	van der Maaten and Hinton, 2008	https://lvdmaaten.github.io/tsne/
R (v3.6.0)	The R Foundation	https://www.r-project.org; RRID: SCR_001905
Python(v2.7.0)	Python Software Foundation	https://www.python.org; RRID: SCR_008394

(*Continued on next page*)

Continued		
REAGENT or RESOURCE	SOURCE	IDENTIFIER
Picard (v2.18.22)	Broad Institute	https://broadinstitute.github.io/picard/; RRID: SCR_006525
Fiji	Schindelin et al., 2012	https://imagej.net/Fiji; RRID: SCR_002285
STAR (v2.7.0a)	Dobin et al., 2013	https://github.com/alexdobin/STAR/releases; RRID: SCR_015899
Other		
Single Cell RNA-Seq Chip 2 (100 μm etch depth), fluorophilic	Dolomite Bio	Cat# 3200543

RESOURCE AVAILABILITY

Lead contact

Further information and requests for resources and reagents should be directed to and will be fulfilled by the Lead Contact, Mark J. Zylka (zylka@med.unc.edu).

Materials availability

This study did not generate new unique reagents.

Data and code availability

The accession number for the raw sequencing data, raw count data, normalized count data, and meta data reported in this paper is GEO: GSE134003. Code for the Shiny web application and histological analyses are available at https://github.com/jkniehaus/Niehaus2021.

EXPERIMENTAL MODEL AND SUBJECT DETAILS

Mice and behavior

All procedures used in this study were approved by the Institutional Animal Care and Use Committee at the University of North Carolina at Chapel Hill. Mice were maintained three to five per cage on a 12 h:12 h light:dark cycle and given food and water *ad libitum*. All conditions were assigned randomly and therefore mice of different conditions were co-housed. Three to four-month-old male C57BL/6 mice were used for all experiments. Studies requiring > 10 total animals (e.g., Drop-seq, liposomal depletion, CD163 overexpression) were performed in two cohorts with equal numbers of mice per condition. No statistical methods were used to predetermine sample size.

Neuropathic pain model

Spared nerve injury (SNI) surgeries were performed under a sterile environment as described previously (Shields et al., 2003). Adult male mice were anesthetized with 2% isoflurane and maintained at 1% isoflurane throughout the procedure. SNI and superficial injury (SI) surgeries were performed on the left hind limb of all mice. A 2 cm incision was made in the skin followed by separation of the biceps femoris muscle to expose the sciatic nerve. For SNI animals, the common peroneal and sural nerves were ligated with 6-0 silk suture and transected distal to the ligature. The injury was then closed with forceps and sealed with surgical clips. In SI animals the nerve was exposed but left unharmed. Animals were monitored daily until euthanasia to ensure proper wound healing.

METHOD DETAILS

Mouse behavior

Mechanical sensitivity measured by von Frey filaments was done using a set of eight filaments that bend at various forces (g): 0.407, 0.692, 1.20, 1.50, 2.04, 3.63, 5.50, 8.50. Each filament was pressed against the hind paw until the pressure either caused the filament to bend (no response) or elicit a withdrawal response. Hindpaw thermal sensitivity was measured using a Plantar Test apparatus (IITC) following the Hargreaves method (Hargreaves et al., 1988). Cutoff time was 20 s. Each animal was measured twice (> 15 minutes between each measurement) and the time to paw withdrawal was averaged. The experimenter was blinded to the animal identity and condition for all behavioral experiments.

Intrathecal injections and dosing

Mice were awake and restrained under a thick cloth for all intrathecal (i.t.) injections. Briefly, the injection area was trimmed of all fur and wiped with 70% ethanol. All i.t. injections were performed using a 25 μL Hamilton syringe with a 27-gauge beveled needle.

Cell depletion experiments were performed using the mannosylated macrophage depletion kit (CLD-8914, Encapsula Nano Sciences). Mice were injected i.t. (10 μL) with saline, empty liposomes, or clodronate-containing liposomes. Specificity of liposomal uptake was assessed by administering 10 μL of m-Fluoroliposome®-DiI (CLD-8924, Encapsula Nano Sciences) via i.t. injection.

Mannosylated polyethylenimine (mPEI) DNA transfections were performed using the *in vivo*-jetPEI®-Man kit (Polyplus, 203-10G). mPEI-DNA complexes were made following the manufacturer's protocol. Briefly, equal parts of plasmid DNA (pDNA) in 5% glucose was mixed with mPEI (N/P ratio of 6) in 5% glucose. The solution was vortexed, incubated at room temperature for 15 minutes, and subsequently administered to mice via i.t. injection. The pDNA composition (by mass) for transfections contained 50% plasmids expressing farnysylated GFP (pGFPf) and 50% plasmids expressing either Flag (pFlag) or the mouse *Cd163* ORF (pCD163). All plasmids used human cytomegalovirus (CMV) promoters and were purchased commercially (pGFPf, Clontech; pCD163, Sino Biological, MG51057-CH) or were made in-house (pFlag). We found that freeze-thaw cycles reduced the transfection efficiency of mPEI nanoparticles. To control for lot-to-lot variability and variation in freeze thaw, we stored mPEI nanoparticles in aliquots sufficient for use in 20 mice, and first tested five different concentrations (n = 2 animals per concentration) *in vivo* to ensure that increased CD163 levels and increased cell number were comparable to that seen in SI injured animals. For cohort 1, animals received a total of 5 μg of pDNA (5 μL total injection; 1 μg/μL). For cohort 2, animals received a total of 1.25 μg of pDNA (5 μL total injection; 0.25 μg/μL).

Single-cell isolation from spinal cord tissue

Animals were anesthetized with pentobarbital and perfused with 95% O_2/5% CO_2 bubbled N-methyl-D-glucamine (NMDG) artificial cerebral spinal fluid buffer (Ting et al., 2014) supplemented with tetrodotoxin (1 μM), 6,7-dinitroquinoxaline-2,3-dione (20 μM), and D-2-amino-5-phosphonovalerate (20 μM, NMDG+) to prevent excitotoxicity during cell dissociation. Lumbar segments of the spinal cord were collected and then were quickly chopped into 1 mm pieces and normalized in chilled, bubbling NMDG+ buffer for 15 minutes. Tissue was transferred to digestion buffer (NMDG+ with 2 mg/mL collagenase and 2 mg/mL protease from *Streptomyces griseus)* prewarmed to 37°C. Tissue was triturated twice (once after 20 minutes and again after 30 minutes) with a 10 mL serological pipette before being spun down at 600 x g for 10 minutes in a prechilled centrifuge (4°C). The supernatant was discarded, and the cell pellet was resuspended and triturated in 1 mL NMDG+ with a fire-polished Pasteur pipette. The cell suspension was added to and mixed with 4 mL of a density gradient solution (1.1 mL Percoll, 2.9 mL NMDG+). Cells were centrifuged at 600 x g for 10 minutes. Cell pellets were resuspended with 1 mL NMDG+, triturated with a fire-polished Pasteur pipette, and passed through a 100 μm filter. A subset of cells were stained with SYTOX Green (Thermo Fisher,1:250 dilution) and counted manually on a hemocytometer. Cells were fixed and stored as described previously (Alles et al., 2017). Briefly, 4 mL of prechilled methanol (−20°C) was added dropwise and the mixture was kept on ice for 15 minutes before being stored in −80°C.

Drop-seq procedure and sequencing

Methanol fixed cells were rehydrated with PBS. Drop-seq and library preparations were performed as described previously with the exception that the initial PCR amplification was increased to 15 cycles (Loo et al., 2019; Shekhar et al., 2016). Libraries from each sample were tagged with Nextera XT Amplification DNA Library Preparation Kit (Illumina) and sequenced on an Illumina HiSeq 4000. Twenty Drop-seq experiments were performed across four days and batch corrected bioinformatically.

Histology

Animals were anesthetized with pentobarbital and then transcranial perfused with pre-chilled PBS followed by freshly made 4% paraformaldehyde (PFA). Lumbar spinal cords were dissected (ensuring meninges remained intact) and post-fixed in PFA overnight. Tissue was then cryoprotected in 30% sucrose for 24 hours before being embedded and frozen in Neg-50 (Thermo Scientific; cat# 25322-68-3). Sections of lumbar segments (L3-L5) were collected and either mounted on Fisher Superfrost Plus slides (cat# 12-550-15) before being stored at −80°C, or kept floating in PBS at 4°C for short-term use. For time point studies and liposome experiments, sections were cut at 20 μm. For *in situ* hybridization experiments, sections were cut at 16 μm. For all other histological experiments, sections were cut at 30 μm.

Sections were washed with PBS three times for five minutes before being blocked with 10% normal donkey serum (NDS) or normal goat serum (NGS) in PBS-T (0.3% Triton) for 30 minutes. Sections were then incubated with primary antibody in 5% NDS/NGS supplemented PBS-T (0.1% Tween) for either two hours (on slide staining) or overnight (floating sections) at room temperature. Sections were washed three times in PBS-T (0.1% Tween) before being incubated in donkey- or goat-conjugated secondary antibodies diluted in PBS for two hours. Sections were washed with PBS, counterstained with DAPI, and mounted (FluoroGel, Electron Microscopy Sciences). For CD163 immunostaining, heat-induced epitope retrieval was performed prior to immunostaining. Briefly, free-floating sections were incubated in 1x citrate buffer (10x Citrate buffer, pH 6.0, Antigen Retriever, Sigma-Aldrich, C9999) at 95°C for 15 minutes before being washed with PBS and subsequent immunostaining.

The following antibodies/concentrations were used: goat polyclonal anti-MRC1/CD206 (R&D Systems, AF2535; 1:200); rabbit monoclonal anti-CD163 (Abcam AB182422; 1:200); rat monoclonal anti-CD31 (PECAM-1) (BD Biosciences, 553370; 1:200); rabbit polyclonal anti-IBA1 (WAKO, 019-19741; 1:400); chicken polyclonal anti-GFAP (Novus Biologicals, NBP1-05198; 1:1000); chicken polyclonal anti-GFP (Aves Labs, GFP-1010; 1:2000); Alexa Fluor 488 donkey anti-goat (Jackson ImmunoResearch Laboratories, 705-545-003; 1:500); Alexa Fluor 488 donkey anti-chicken (Jackson ImmunoResearch Laboratories, 703-545-155; 1:500); Cy3

donkey anti-rat (Jackson ImmunoResearch Laboratories, 712-165-153; 1:500); Alexa Fluor 647 donkey anti-rabbit (Invitrogen, A-31573; 1:500); Alexa Fluor 647 donkey anti-chicken (Jackson ImmunoResearch Laboratories, 703-605-155; 1:500).

To label cycling cells, 80 μg 5-ethynyl-2′-deoxyuridine (EdU) in 100 μL of saline was administered by intraperitoneal (i.p.) injection once a day for four consecutive days. Following immunohistochemistry, tissue was treated with an EdU reaction solution (1.6 μM Alexa 488-azide, 4 μM $CuSO_4$, 100 mM sodium ascorbate, 10 mM Tris pH 8.5 in PBS) for 30 minutes at room temperature before being washed with PBS and mounted.

For *in situ* hybridization, the RNAscope Fluorescent Multiplex Assay (Advanced Cell Diagnostics, 320851) was performed following target retrieval according to the manufacturer's protocol. Briefly, slides were dried at 60°C for 30 minutes and post-fixed in cold 4% PFA for 15 minutes. Slides were subsequently dehydrated in 50%, 70%, and 100% ethanol and allowed to air dry for 5 minutes at room temperature. Slides were then submerged in boiling 1x Target Retrieval buffer (Advanced Cell Diagnostics, 322000) for 5 minutes. Slides were briefly washed with room temperature distilled water, rinsed with 100% ethanol, and sections outlined with a hydrophobic pen (ImmEdge, Vector Labs). Finally, slides were pretreated with RNAscope Protease and allowed to incubate for 30 minutes at 40°C in a humidified hybridization oven before continuing with the RNAscope Fluorescent Multiplex Reagent Kit protocol (Document Number 320393-USM) using probes targeting *Mrc1* (Advanced Cell Diagnostics, 317261) and *Il10* (Advanced Cell Diagnostics, 437511-C3). To capture *in situ* hybridization signal, z stack images were acquired with a 63x oil immersion objective for every cell expressing *Mrc1* in a given section.

Image analysis/quantification

Z stack images were acquired with a Zeiss LSM 710 confocal microscope. Microscope settings were consistent between conditions. Images were imported into Fiji for quantification (Schindelin et al., 2012). Prior to quantification, z stacks were flattened to a maximum intensity projection. MMs and PVMs were differentially identified based on anatomical location. For all spinal macrophage analyses, only spinal sections with intact pia mater were included. To assess cell numbers, z stack tile images of the entire section (MMs and PVMs) or the ipsilateral dorsal horn (microglia, astrocytes) were acquired with a 20x objective. A DAPI mask of the stitched maximum intensity projection image was then overlaid on the channel of the protein of interest (e.g., MRC1 or IBA1), and the number of nuclei positive for the protein of interest were counted. For CD163 colocalization experiments, 8-10 z stack images of $MRC1^+$ macrophages were acquired per section in with a 40x oil immersion objective. To quantify CD163 expression in $MRC1^+$ macrophages, masks were generated from the MRC1 channel and the percent of overlapping area with the CD163 channel was calculated. *In situ* hybridization images were acquired with a 63x oil immersion objective and the signal was quantified following the manufacturer's guidelines (Advanced Cell Diagnostics, SOP 45-006). Briefly, maximum intensity projections were produced from z stack images. Background intensity was measured and subtracted from each image before region of interests (ROIs) were drawn using based on DAPI channel for cells containing > 3 dots in the *Mrc1* channel (a cell's signal was considered lipofuscin and therefore was not used if its pattern was present across multiple channels). A mask of the *Il10* channel was then generated using the automatic threshold tool in Fiji (default algorithm), and the number of dots per cell was quantified. All histological quantification data can be found in Table S4. Additional information on image analysis and example code can be found at https://github.com/jkniehaus/Niehaus2021.

QUANTIFICATION AND STATISTICAL ANALYSIS

Statistical analyses and data visualization were performed in Excel and R. Statistical details (sample number, test used, and comparison details) can be found in figure legends. Sample numbers (n) indicate individual animals with the exception of Figure 2E, where n pertains to cells. For behavioral data, p values were generated by comparing SI and SNI groups at each force (Figures 1B, 3D, 4E, S5C, S5D, and S5G) or time point (Figures 4F and S1A) via two-sided Student's t tests. The resulting p values were corrected using Holm-Bonferroni multiple comparisons method. For histological experiments where multiple sections were analyzed from each animal, the average was taken to summarize multiple sections. Complete information on histological experiments (both individual sections and average values per animal) can be found in figure legends and Table S4. Two-sided Student's t tests, Holm-Bonferroni false discovery rate corrections, and two-way ANOVAs with Tukey's HSD post hoc analysis for pairwise confidence intervals were used as indicated in figure legends. Line graphs are presented as the mean ± standard error of the mean. Boxplot whiskers extend to the highest/lowest value within ± 1.5 x inter quartile range. Example code for scRNA-seq analysis, ANOVAs, and data visualization can be found at https://github.com/jkniehaus/Niehaus2021. Experimental groups were considered significant if $p < 0.05$.

Processing and alignment of Drop-seq data

Raw reads were processed based on the Drop-seq Toolkit v1.12 (Macosko et al., 2015; Shekhar et al., 2016) to identify and sort unique cells and unique molecular identifiers (UMIs) with corresponding exonic reads. Processed reads were aligned to a mm10-hg19 hybrid genome using STAR (Dobin et al., 2013). Uniquely mapped reads were retained, and short or multi-mapped reads were discarded. Barcoded beads missing a base in their cell barcode were corrected as described in Drop-seq tools v1.12 (http://mccarrolllab.org/wp-content/uploads/2016/03/Drop-seqAlignmentCookbookv1.2Jan2016.pdf) (Shekhar et al., 2016; Loo et al., 2019).

Cell barcodes were determined to be species-specific if > 90% of the transcripts came from that species or were considered a doublet if neither species achieved 90% specificity. Cell barcodes were not considered if the transcript count sum (mouse+human) was less than 500. Gene expression matrices were then created using mouse-specific UMIs.

Basic cell/gene filtration and cell clustering

Cells expressing fewer than 400 unique genes or greater than 10% mitochondrial transcripts were removed. Genes were removed if they were not expressed in at least 30 cells with at least 3 transcripts. Technical batches were corrected in two rounds using ComBat (Johnson et al., 2007) based on Drop-seq day and animal cohort. The resulting batch-corrected gene expression matrix was median-centered and log-transformed to generate our final dataset (termed "Normalized expression" used throughout the text).

Cell clusters were established based on significant principal components (PCs, n = 60), whose eigenvalues were greater than those generated from randomly permutating the dataset (n = 1,000). Louvain clustering was performed with a silhouette score-optimized (Euclidean distance between each cell and the centroid of a given cluster) nearest neighbor parameter (Loo et al., 2019; Shekhar et al., 2016). This resulted in 20 cell clusters.

To resolve cell types with more specificity, the above pipeline was performed a second time on each of the initial 20 clusters. The second clustering iteration was identical to the first with two key cluster refinement exceptions. First, a set of oligodendrocyte-related genes were removed for the second round of clustering (apart from the two initial clusters that were classified as oligodendrocytes) in order to remove signal caused by myelin debris. Second, clusters lacking at least one marker gene (enriched by > 1.0 $\log_{10}$ fold-change compared to other clusters) were merged with the next most similar cluster (Pearson correlation). This resulted in 69 transcriptionally distinct clusters. After annotating each of the 69 clusters, three low-quality clusters were removed based on signs of doublets (expressing genes from two cell types), resulting in 66 final clusters.

The 66 final clusters were classified into seven principal cell types based on their distance from one another. A Pearson correlation distance ($d = 1 - r$) was computed between each cluster where d is correlation distance and r is Pearson's correlation coefficient of the average normalized gene expression between two clusters. Clusters with a distance equal to or less than 1 were classified into the same principal cell type.

Identification of marker genes and differentially expressed genes

Binomial tests were used to identify cell markers based on the presence or absence of a given gene's expression, as described previously (Shekhar et al., 2016). Briefly, this test determines the expression frequency of a given gene g across cells in one population (N cells) compared to a second, reference population (M cells). As defined previously (Shekhar et al., 2016) the p value for this was computed using the following formula

$$p_g = \sum_{k=N_g}^{N} \binom{N}{k} \gamma^k (1-\gamma)^{N-k}$$

where $\gamma = M_g / M$ refers to the presence frequency in the reference population. We determined cell type identities by testing for gene enrichment in one cell type compared to all others and correlating these markers with previously published datasets (Zeisel et al., 2018). We identified cell type-specific genes by comparing gene enrichment in one cell type with others that are hierarchically similar (e.g., Pericytes1 versus Pericytes2 and Pericytes3; hierarchical similarity determined by Pearson's distance).

Similar to marker genes, differentially expressed genes were obtained using a binomial test (Shekhar et al., 2016) to compare SI and SNI cells within each cell type.

To correct for variability and effect size, we required differentially expressed genes to have an FDR-corrected binomial q-value < 0.05 as well as a $\log_2$-fold change of > |0.5|. This threshold yielded robust differences in gene expression between SI and SNI animals and is optimal for identifying gene expression differences with zero-inflated data, like scRNaseq data. Functional gene ontology analysis was performed on differentially expressed genes from Macro1 and Macro2 cells using ToppFun using a significance cuttoff of 0.05 (Bonferroni & Holm corrected false discovery rate) (Chen et al., 2009).

Comparisons to other published scRNaseq datasets

To compare our data to published single-cell/nuclei neuron clusters, average expression values were calculated for every gene from our dataset as well as those made available (Häring et al., 2018; Sathyamurthy et al., 2018). First, we subset the genes used based on variability (standard deviation greater than 0.1). Genes were removed if they were not present in all three datasets. Pearson correlation coefficients were calculated between clusters from our study and neuron clusters from Sathyamurthy et al. 2018 and Haring et al. 2018. The resulting matrix of correlation coefficients were plotted as heatmaps.

Neuron, Volume *109*

Supplemental information

Spinal macrophages resolve nociceptive hypersensitivity after peripheral injury

Jesse K. Niehaus, Bonnie Taylor-Blake, Lipin Loo, Jeremy M. Simon, and Mark J. Zylka

Supplemental Figures:

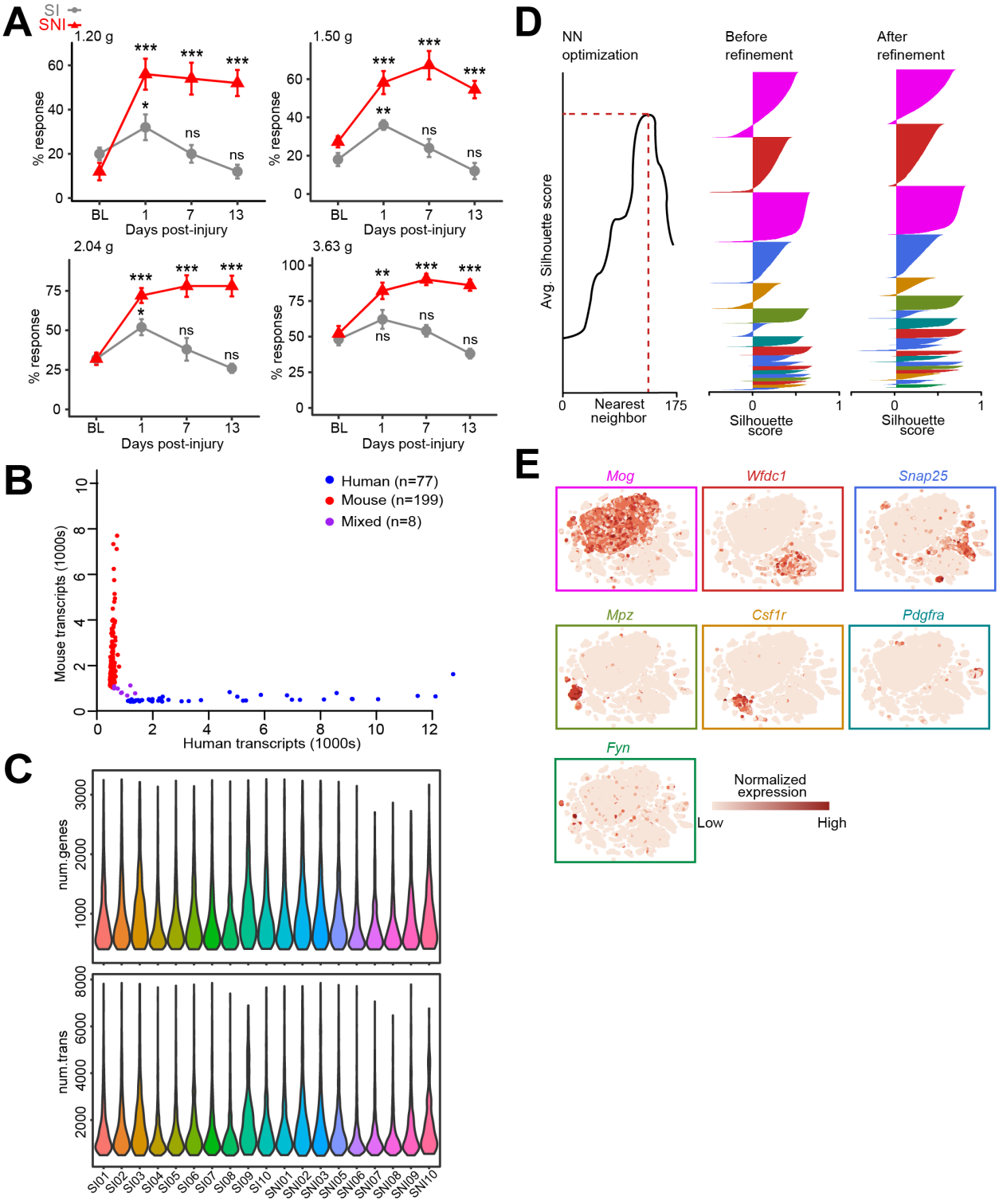

Figure S1 (Related to Figure 1). Mechanical sensitivity changes over time in SI and SNI mice, and benchmarks for scRNAseq viability, data analysis, and cell composition.

(A) Mechanical sensitivity between SI and SNI animals over time using different VF filaments. n = 10 animals per condition. Mean ± s.e.m. Bonferroni-Holm corrected two-sided *t*-tests compared to baseline (BL). *P < 0.05, **P < 0.01, ***P < 0.001. ns = not significant.

(B) Representative barnyard plot of species-specific scRNAseq with mouse spinal cord and human embryonic kidney cell spike-ins. Species indicated if 90% or more transcripts came from a single species, otherwise classified as “mixed.”

(C) Violin plots showing the number of unique genes and transcripts expressed in cells across each sample. n = 10 and 9 samples from SI and SNI animals, respectively

(D) Louvain clustering optimization of the initial 20 clusters based on nearest-neighbor (NN) optimization (left) and silhouette score refinement (mid, right). The nearest neighbor parameter resulting in the highest average silhouette score was chosen. Silhouette scores calculated from Euclidean distance to a given cluster’s centroid. Clusters color-coded by principal cell type from Figure 1.

(E) tSNE plots of all cells expressing marker genes of the seven principal cell types.

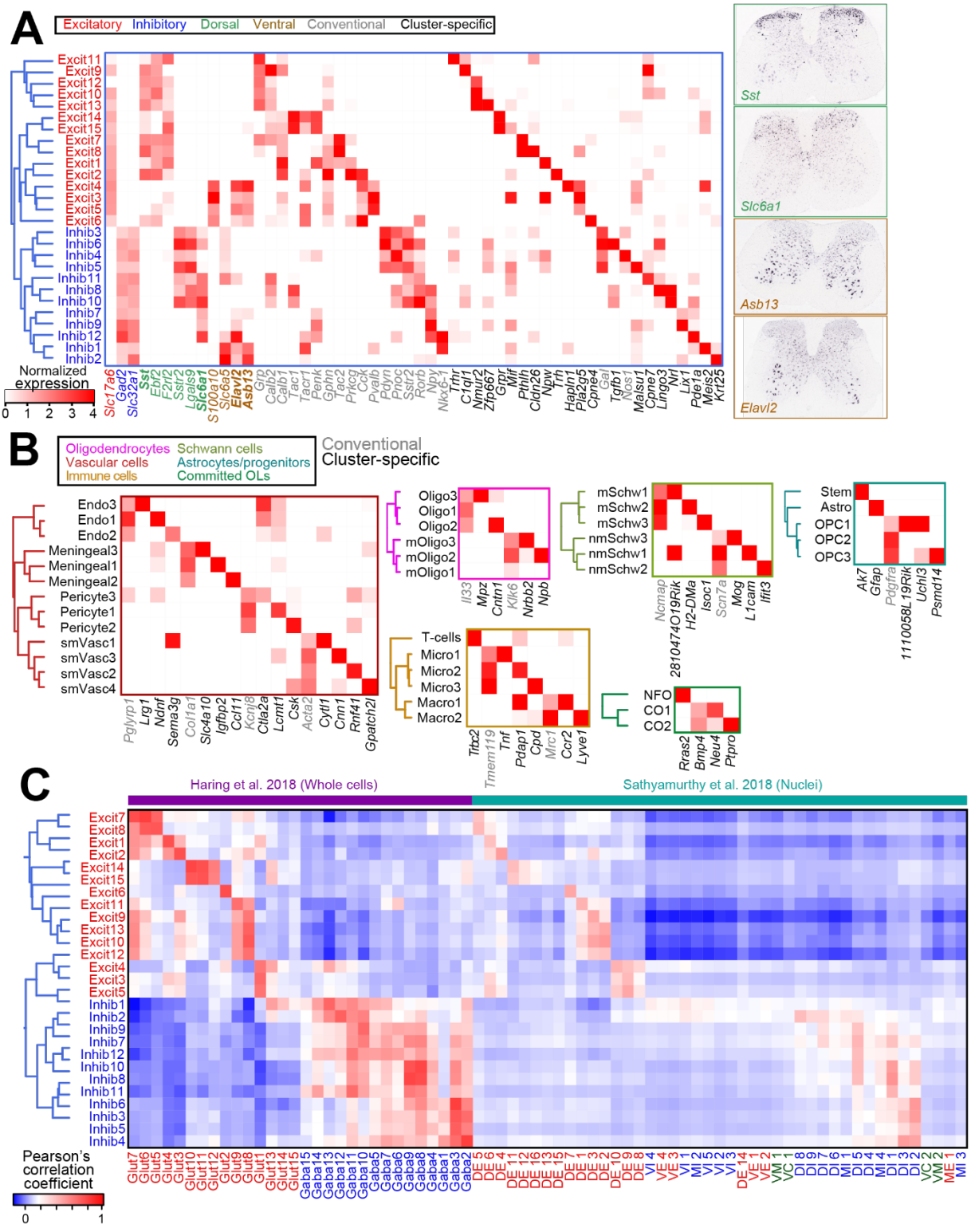

Figure S2 (Related to Figure 1). Transcriptomic characterization of spinal cord cell types and comparison with published datasets.

(A) (Left) Heatmap of gene expression (average transcripts per million) for neuronal cell types ordered by relatedness (dendrogram, Pearson correlation coefficient). (Right) *In situ* hybridization of dorsal- and ventral- specific genes of the adult lumbar spinal cord from the Allen Brain Atlas (mousespinal.brain-map.org). Excit = Excitatory. Inhib = Inhibitory.

(B) Heatmap of normalized gene expression across non-neuronal cells. Endo = Endothelial. smVasc = Smooth muscle vasculature. Oligo = Oligodendrocyte. mOligo = Myelinating oligodendrocyte. mSchw = Myelinating Schwann cell. nmSchw = Non-myelinating Schwann cell. Stem = Stem/Ependymal cell. Astro = Astrocyte. OPC = Oligodendrocytic precursor cell. Micro = Microglial. Macro = Macrophage. NFO = Newly formed oligodendrocyte. CO = Committed oligodendrocyte.

(C) Heatmap of the average normalized gene expression from our spinal neuron cell types and those generated from Haring et al. 2018 and Sathyamurthy et al. 2018.

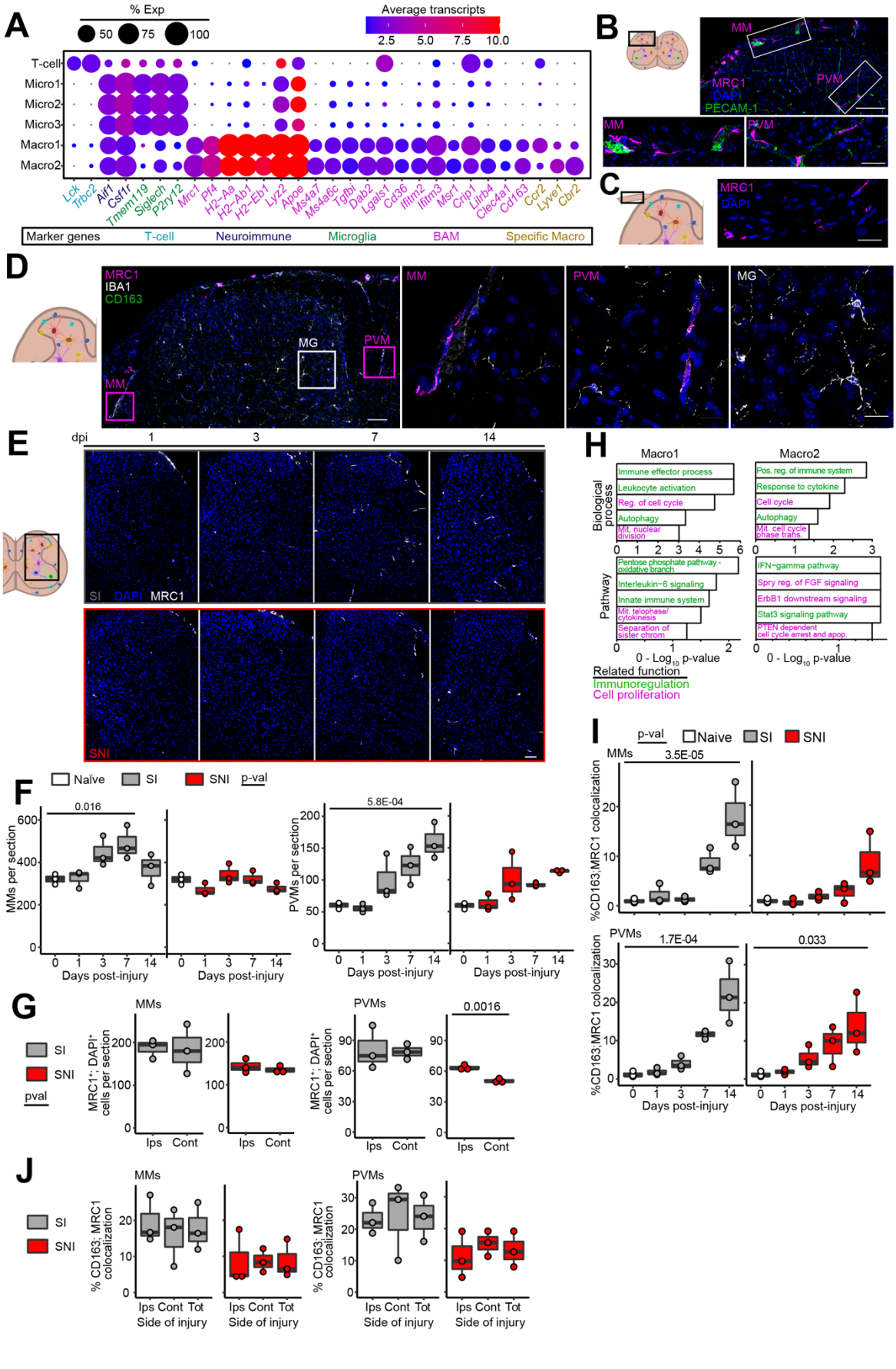
A
% Exp
50 75 100
Average transcripts
2.5 5.0 7.5 10.0
T-cell
Micro1
Micro2
Micro3
Macro1
Macro2
Lck Trbc2 Aif1 Csf1r Tmem119 Siglech P2ry12 Mrc1 Pf4 H2-Aa H2-Ab1 H2-Eb1 Lyz2 Apoe Ms4a7 Ms4a6c Tgfbi Dab2 Lgals1 Cd36 Ifitm2 Ifitm3 Msr1 Crip1 Lilrb4 Clec4a1 Cd163 Ccr2 Lyve1 Cbr2
Marker genes T-cell Neuroimmune Microglia BAM Specific Macro
B
MM
MRC1
DAPI
PECAM-1
PVM
C
MRC1
DAPI
D
MRC1
IBA1
CD163
MG
PVM
MM
E
dpi 1 3 7 14
SI DAPI MRC1
SNI
F
Naïve SI SNI p-val
0.016
5.8E-04
MMs per section
PVMs per section
Days post-injury
G
SI
SNI
pval
MMs
PVMs
MRC1+; DAPI+ cells per section
0.0016
Ips Cont
H
Macro1
Macro2
Biological process
Immune effector process
Leukocyte activation
Reg. of cell cycle
Autophagy
Mit. nuclear division
Pos. reg. of immune system
Response to cytokine
Cell cycle
Autophagy
Mit. cell cycle phase trans.
Pathway
Pentose phosphate pathway - oxidative branch
Interleukin-6 signaling
Innate immune system
Mit. telophase/ cytokinesis
Separation of sister chrom.
IFN-gamma pathway
Spry reg. of FGF signaling
ErbB1 downstream signaling
Stat3 signaling pathway
PTEN dependent cell cycle arrest and apop.
0 - Log10 p-value
Related function
Immunoregulation
Cell proliferation
I
p-val
Naive SI SNI
MMs
3.5E-05
PVMs
1.7E-04
0.033
%CD163;MRC1 colocalization
Days post-injury
J
SI
SNI
MMs
PVMs
% CD163; MRC1 colocalization
Ips Cont Tot
Side of injury

Figure S3 (Related to Figure 2). Spinal macrophage transcriptomic characterization, cell marker specificity, and phenotypic changes following SI or SNI.

(A) Dot plots summarizing gene expression of neuroimmune cell markers. nTrans = Average number of transcripts per cell. % Expr = Percentage of cells expressing the corresponding gene. BAM = Border associated macrophage.

(B) Representative images of MMs and PVMs expressing MRC1 in the lumbar spinal cord. Top right scale bar = 100 μm. Bottom right scale bar = 20 μm.

(C) Representative image of MRC1 expression in dorsal root macrophages. Scale bar = 20 μm.

(D) Representative low (far left) and high (three right) magnification images delineating $MRC1^+$ macrophages and $IBA1^+$ microglia. MG = microglia. Left scale bar = 100 μm**.** Right scale bar = 20 μm.

(E) Representative images of PVMs in lumbar grey matter at 1, 3, 7, and 14 dpi in SI and SNI animals. Scale bar = 100 μm.

(F) Quantification of MMs (left) and PVMs (right) per section over time separated by condition. Data replotted from Figure 2B. Tukey's HSD-adjusted p-values. P-values only shown if < 0.05. Consecutive datapoints within $1/30^{th}$ of the range are binned.

(G) Quantification of MMs (left) and PVMs (right) in SI and SNI animals at 14 dpi ipsilateral (Ips) and contralateral (Cont) to the side of injury. n = 3 animals per condition. P-values < 0.05 are displayed, two-sided *t*-tests. Consecutive datapoints within $1/30^{th}$ of the range are binned.

(H) Cell cycle and immunoregulatory gene ontology (GO) terms downregulated in SNI Macro1 and Macro2 cells relative to SI at 14 dpi. Complete list of input genes and GO terms in Table S3.

(I) Quantification of CD163;MRC1 colocation in MMs (top) and PVMs (bottom) over time. Data replotted from Figure 2G. Tukey's HSD-adjusted p-values. P-values only shown if < 0.05. Consecutive datapoints within 1/30th of the range are binned.

(J) Quantification of CD163;MRC1 colocalization laterality (Ips = Ipsilateral to injury; Cont = Contralateral to injury; Tot = Total) in MMs (left) and PVMs (right) at 14 dpi. Consecutive datapoints within 1/30th of the range are binned.

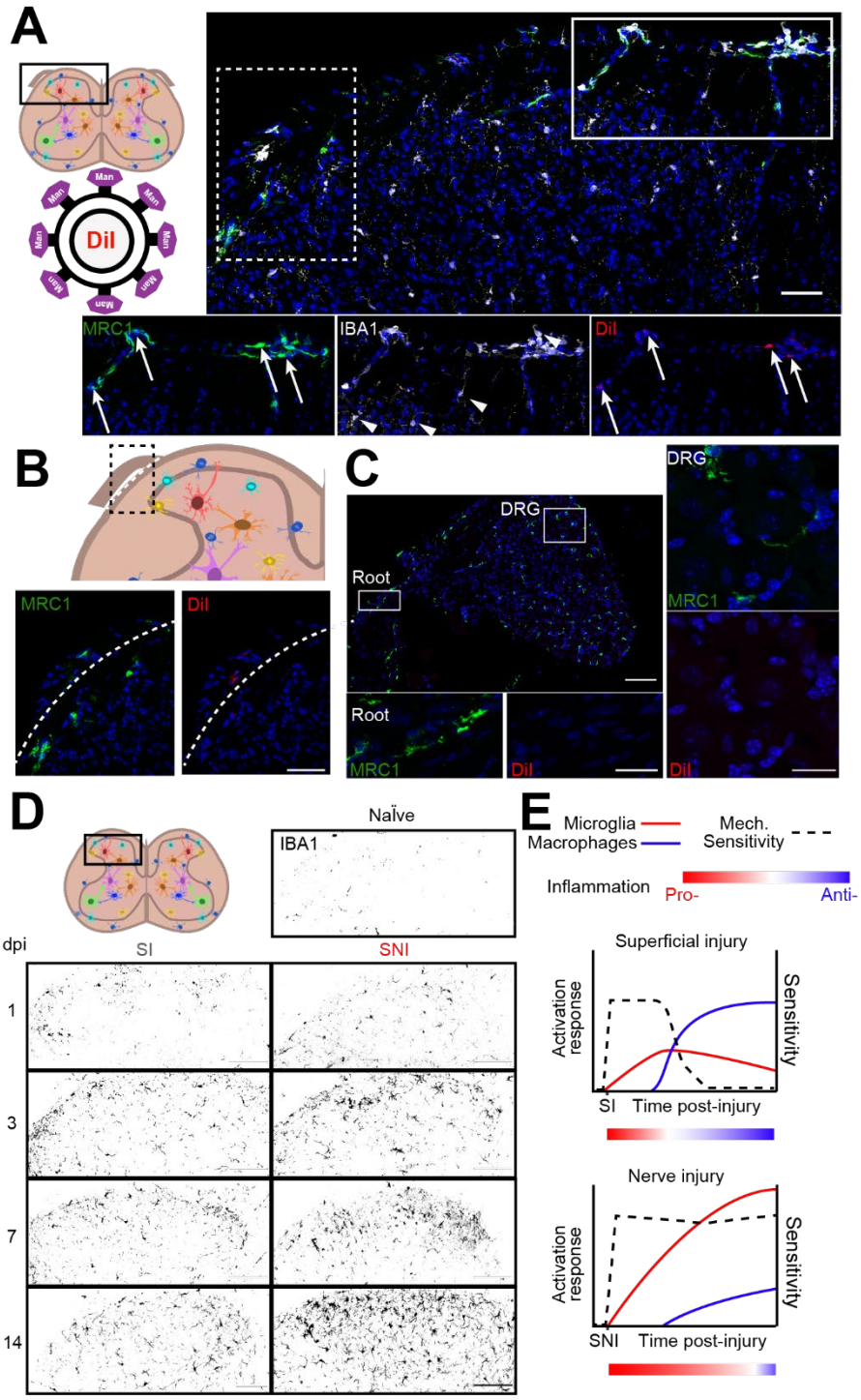

Figure S4 (Related to Figure 3). Targeted uptake of mannosylated liposomes in MRC1^{+} macrophages and microgliosis in SI and SNI animals over time.

(A) Representative images of lumbar spinal cord 3 days post-injection of DiI-encapsulated mannosylated liposomes. Arrows, DiI^+ MMR^+ $IBA1^+$ macrophages. Arrowheads, DiI^- MMR^- $IBA1^+$ microglia. Scale bar = 50 μm.

(B) Representative images from Figure S4A of attached dorsal roots. Dotted line indicates separation of spinal cord and roots. Scale bar = 20 μm.

(C) (Top left) Low magnification image of lumbar DRG 3 days post-injection of DiI-encapsulated mannosylated liposomes. High magnification of DRG (right) and attached roots (left). Top left scale bar = 100 μm. Bottom scale bars in C = 10 μm.

(D) Representative images of IBA1 staining in the dorsal horn of naïve, SI, and SNI animals at 1, 3, 7, and 14 dpi. Scale bar = 100 μm.

(E) Temporal correlation between neuroimmune cell activation (microglia and $MRC1^+$ macrophages) and mechanical (mech.) sensitivity following superficial injury and nerve injury. Schematic based on data in our current paper and the literature. Schematic is illustrative, meaning magnitude changes and temporal changes are approximate.

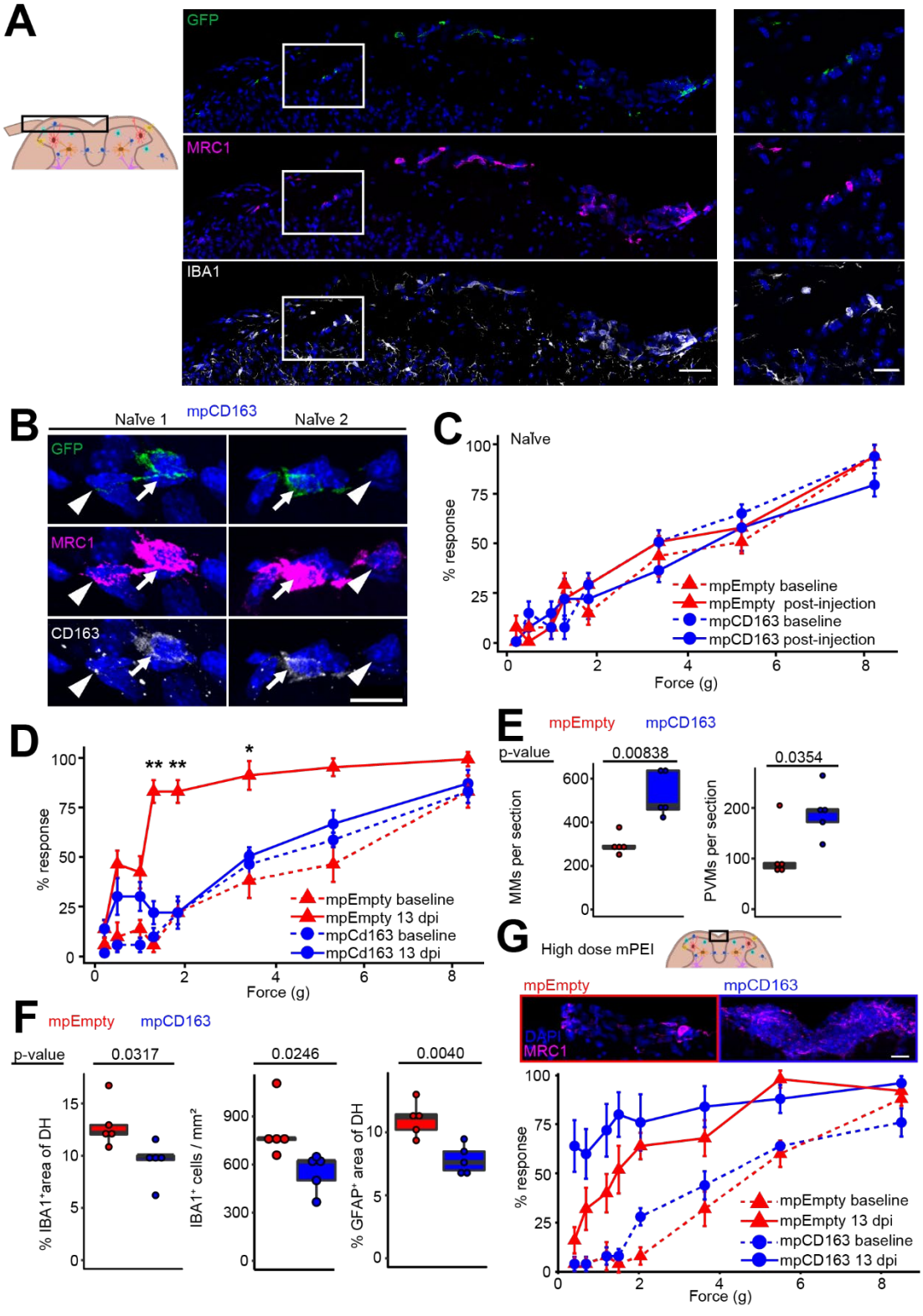
A
GFP
MRC1
IBA1
B
Naïve 1
mpCD163
Naïve 2
GFP
MRC1
CD163
C
Naïve
% response
Force (g)
mpEmpty baseline
mpEmpty post-injection
mpCD163 baseline
mpCD163 post-injection
D
** **
*
% response
Force (g)
mpEmpty baseline
mpEmpty 13 dpi
mpCd163 baseline
mpCd163 13 dpi
E
mpEmpty
mpCD163
p-value
0.00838
0.0354
MMs per section
PVMs per section
F
mpEmpty
mpCD163
p-value
0.0317
0.0246
0.0040
% IBA1⁺area of DH
IBA1⁺ cells / mm²
% GFAP⁺ area of DH
G
High dose mPEI
mpEmpty
mpCD163
DAPI
MRC1
% response
Force (g)
mpEmpty baseline
mpEmpty 13 dpi
mpCD163 baseline
mpCD163 13 dpi

Figure S5 (Related to Figure 4). Mannosylated PEI specificity, additional data supporting targeted CD163 expression, reproducibility of low dose mpCD163 in a second cohort, and effects of high dose mpCD163.

(A) (Left) Representative images of mPEI transfection pattern (GFP) in the spinal dorsal horn 10 days post-treatment. Scale bar = 50 μm. (Right) High magnification image of boxed area. Scale bar = 20 μm.

(B) Representative images of CD163 and GFPf expression in MMs transfected (arrows) and not transfected (arrowheads) with mpCD163. Scale bar = 15 μm.

(C) Mechanical sensitivity in naïve animals before and 10 days after either empty (mpEmpty) or CD163 (mpCD163) treatment. n = 3 animals per condition. Mean ± s.e.m.

(D) Mechanical sensitivity in a second cohort of animals at baseline and 13 days post SNI injury (dpi) after either mpEmpty (n = 5) or mpCD163 (n = 5) treatment. Mean ± s.e.m. Bonferroni-Holm corrected two-sided *t*-tests between conditions at 13 dpi. *P < 0.05, **P < 0.01.

(E) Quantification of MMs and PVMs 14 dpi in mpEmpty or mpCD163 treated animals. n = 5 animals per condition, 1 section per animal. P-values, two-sided *t*-tests. Consecutive datapoints within 1/30th of the range are binned.

(F) Quantification of IBA1 area, the number of IBA1^{+} cells, and GFAP area 14 dpi after mpEmpty or mpCD163 treatments. n = 5 animals per condition, 1 section per animal. P-values, two-sided *t*-tests. Consecutive datapoints within 1/30th of the range are binned.

(G) (Top) Representative images of MMs 14 dpi after high-dose treatment of mpEmpty (top) and mpCD163 (bottom). Scale bar = 20 μm. (Bottom) Mechanical sensitivity at baseline and 13 dpi after high-dose treatment of either mpEmpty or mpCD163. n = 5

animals per condition. Mean ± s.e.m. No statistically significant differences between mpEmpty and mpCD163 groups.